Durham University

Durham E-Theses

THERMAL ENERGY CONVERSION USING NANO RECTENNA ARRAYS (THE MAIN FOCUS IS ON THE AUTOMOTIVE SECTOR).

UKE, IGNATIUS,DOUGLAS,OZOEMENA

How to cite:

UKE, IGNATIUS,DOUGLAS,OZOEMENA (2019) *THERMAL ENERGY CONVERSION USING NANO RECTENNA ARRAYS (THE MAIN FOCUS IS ON THE AUTOMOTIVE SECTOR).*, Durham theses, Durham University. Available at Durham E-Theses Online: http://etheses.dur.ac.uk/13562/

Use policy

This work is licensed under a Creative Commons Public Domain Dedication 1.0 (CC0)

Academic Support Office, Durham University, University Office, Old Elvet, Durham DH1 3HP
e-mail: e-theses.admin@dur.ac.uk Tel: +44 0191 334 6107
http://etheses.dur.ac.uk

THERMAL ENERGY CONVERSION USING NANO RECTENNA ARRAYS
(THE MAIN FOCUS IS ON THE AUTOMOTIVE SECTOR).

Ignatius Douglas Ozoemena Uke

A Thesis presented for the degree of
Master of Science by Research

Department of Engineering
Durham University
United Kingdom.

October, 2019

THERMAL ENERGY CONVERSION USING NANO RECTENNA ARRAYS

(THE MAIN FOCUS IS ON THE AUTOMOTIVE SECTOR).

ABSTRACT

This research work is concerned with the study, design and fabrication of an energy harvester for converting radiant heat to electricity using rectenna technology, with key application being on the automobiles. A review of previous works of other researchers is presented, and the main limitations hindering the realisation of a practical and functional rectenna device as well as the main factors for optimising device performance highlighted. The temperature profile of an automobile engine and exhaust was measured in order to determine the operable temperature ranges, which is a key factor when determining the optimum device dimension. The contact angles made by a 5μl drop of water on surfaces coated with different self-assembled monolayers (SAMs) were measured in order to determining the hydrophilicity and hydrophobicity of the surfaces. This gives an idea the surface energy of the dielectric films, thus giving an indication of how uniform a surface coated with such dielectric film will be. Finally, a setup for the low frequency characterisation of the diode was made and validated using ordinary diodes.

DEDICATION

This piece of work is dedicated to

my Wife
Mrs. Onyinye E. Uke

and Children
Adaeze-Jesus Uke, Chinwendu Michelle Uke, Chukwukutelu Chikayima Uke

ACKNOWLEDGEMENT

I remain forever grateful to the ALMIGHTY GOD, THE GOOD LORD, for HIS grace has been so sufficient for me.

I am also very indebted to the following people: My Supervisors in the persons of Dr. Michael D. Cooke, Dr. Claudio Balocco, and Dr. Andrew J. Gallant whose painstaking directions, tireless guidance and thoughtful magnanimity towards my health, have helped me a lot in achieving this feat.

Dr. Chris Pearson, whose jokes and real-time encouraging words in the cleanroom I shall not forget easily.
.....are you sure you are not hiding on purpose? ....No Sir, I'm not hiding at all.

Professor Dagou Zeze for his jokes, especially during the cold winter days of 2018, which makes me to bend down while laughing.
…… Prof., I have a winter coat.

The departmental Postgraduate research director, Prof. John Brigham who has a good listening ear.

Mrs Debra Smith and Becky Mollon for their wonderful assistance during the admission offer deferment and visa processing stages.

All colleagues and friends both within the department and the University at large, it's been a wonderful pleasure and experience knowing and working with you all.

The chief diabetic nurse at Claypath and University medical centre, Mrs Andrea Picton, for her very passionate care, and all members of staff of the diabetic clinic, University Hospital of North Durham, for their so-bright smiles and kind words.

My employer, the University of Abuja, and TETFund, an organ of the Nigerian Government, whose financial, educative and supportive resources were rendered to me in an inestimable measure through the payment of my salaries and the scholarship award offered to me.

Finally, my family members, I must not forget you; though far away, each night, you've been providing me with a very warm family atmosphere that enhanced my zeal all this while. I can only say GOD bless you.

Ignatius Douglas Ozoemena Uke.

Declaration

The work in this thesis is based on research carried out in the department of Engineering, Durham University, England. No part of this thesis has been submitted elsewhere for any other degree or qualification and it is all my own work unless referenced to the contrary in the text.

© Copyright 2019, Ignatius Douglas Ozoemena Uke

The copyright of this thesis rests with the author. No quotations from it should be published without the author's prior written consent and information derived from it should be acknowledged.

CONTENTS

TITLE ……………………………………………………………………………………... i

ABSTRACT………………………………………………………………………...…ii

DEDICATION……………………………………………………………………...…iii

ACKNOWLEDGMENT……………………………………………………………....iv

DECLARATION………………………………………………..............................… v

TABLE OF CONTENT.. vi

LIST of FIGURES.. viii

LIST of TABLES..x

CHAPTER 1 INTRODUCTION…………………………………………………… 1

1.1 Energy Harvesting..1

1.2 Motivation..1

1.2.1 Temperature profile Measurement of an Automobile Engine and Exhaust...2

1.3 Thermal Energy……………………………………………………………………..4

1.3.1 Thermophotovoltaic devices…………………………………………………..5

1.3.2 Thermoelectric devices………………………………………………………... 6

1.4 The Rectenna.. 7

1.4.1 Rectenna Dimensions and Temperature Ranges...13

1.4.2 Rectenna Figures of Merit... 14

CHAPTER 2 THEORY AND BACKGROUND OF STUDY……………………………..17

2.1 Rectification..17

2.1.1 The self-switching diode..17

2.1.2 The Schottky Diode.. 17

2.1.3 Metal-insulator-metal (MIM) diodes.. 18

2.2 Previous Research Works... 19

CHAPTER 3 CONDUCTION MECHANISMS AND NUMERICAL SIMULATION…... 25
3.1 Conduction Mechanisms within a Metal-Insulator-Metal (MIM) Diode………….. 25
3.1.1 Direct Electron Tunnelling………………………………………………… 26
3.1.2 Fowler-Nordheim (F-N) Tunnelling……………………………………….. 27
3.1.3 Schottky emission……………………………………………………….. 28
3.1.4 Poole-Frenkel (P-F.) Emission……………………………….................29
3.1.5 Hopping Conduction……………………………………………………..30
3.2 Numerical Simulation of Charge Transport across the Dielectric Layer…………...32
3.2.1 Estimation of the barrier heights of an asymmetric MIM tunnel junction.....35

CHAPTER 4 DEVICE FABRICATION...46
4.1 Fabrication Processes..46
4.1.1 Wafer processing...46
4.1.2 Insulator preparation and deposition...46
4.1.3 Determination of water contact angles (WCA)..47
4.1.4 Atomic force microscope (AFM) imaging..48
4.2 Process steps for MIM junction fabrication...52
4.2.1 Diagrammatic representation of the device fabrication processes.................55

CHAPTER 5 INSTRUMENTATION FOR DIODE CHARACTERISATION....................58
5.1 Low frequency (LF) Characterisation..58
5.2 Validation of low frequency measurement setup..60

CHAPTER 6 CONCLUSIONS AND FUTURE WORK..64
6.1 Conclusion...64
6.2 Future work...64
6.2.1 Terahertz Characterisation...65

REFERENCES...66

LIST of FIGURES

Figure 1.1: Parts of the engine and exhaust with the respective thermal images................. 4

Figure 1.2: Temperature variation of the spectral emissive power of a blackbody...............5

Figure 1.3: A schematic diagram of thermoelectric effect in a thermoelectric Device......... 7

Figure 1.4: A simple rectenna element and heat source.. 8

Figure 1.5: A schematic of a typical bowtie antenna...9

Figure 1.6: PSD curve of the rectenna showing the region of available convertible power...10

Figure 1.7: An equivalent circuit diagram of the rectenna device...10

Figure 2.1: A molecule of the organic insulator (Octadecyltrichlorosilane)..........................19

Figure 3.1: Schematic energy band diagram of a positively biased MIM diode....................25

Figure 3.2: Schematic energy band diagram of an MIM diode showing Direct tunnelling...27

Figure 3.3: Schematic energy band diagram of an MIM diode showing F-N tunnelling...28

Figure 3.4: Schematic energy band diagram of an MIM diode showing Schottky emission...29

Figure 3.5: Schematic energy band diagram of an MIM diode showing P-F emission...30

Figure 3.6: Schematic energy band diagram of an MIM diode showing Hopping tunnelling...31

Figure 3.7: Schematic energy band diagrams showing forward and reverse biased conditions...36

Figure 3.8: Plots showing the I-V characteristics of fabricated MIM diodes............................43

Figure 3.9: A plot of log ($|I/(V+\Delta ht)^2|$) vs. $1/(V+\Delta ht)$...44

Figure 4.1: 5µl drop of water on a coated and uncoated wafer surface....................................47

Figure 4.2: Surface topography images of wafers coated with SAMs and plain borosilicate glass...50

Figure 4.3: Schematic of TUNA scan configuration and images...51

Figure 4.4: A pictorial representation of the bi-layer fabrication process steps........................56

Figure 5.1: Schematic circuit representation of low frequency characterisation of the diode...60

Figure 5.2: Pictorial representation of the actual setup used for the Characterisation................60
Figure 5.3: The I-V characteristics used in validating the low frequency measurement setup for Zener diode..62
Figure 5.4: The I-V characteristics used in validating the low frequency measurement setup for 1N4007 junction diode..63
Figure 6.1: Terahertz Characterisation setup for the rectenna device..65

LIST of TABLES

Table 1.1: Key engine parameters for the Volkswagen 1.9 litres diesel engine used.......... 2
Table 1.2: Automobile temperature profile measurement values..3
Table 1.3: Advantages and Disadvantages of the thermophotovoltaic and thermoelectric devices...7
Table 1.4: Quantum cut-off frequency and wavelength of automobile engine......................13
Table 1.5: Quantum cut-off frequency and wavelength of automobile exhaust....................14
Table 2.1: A summary of some previous relevant research works with their Limitations.....23
Table 3.1: Experimental data of some fabricated asymmetrical MIM diodes.......................39
Table 4.1: Water droplet contact angles on the respective wafer surfaces.............................48
Table 4.2: RMS roughness of plane borosilicate glass and insulator-coated Wafers.............52
Table 4.3: Spin-coating Conditions and Timing..55

CHAPTER 1

INTRODUCTION

This work aims to study an energy harvester, and develop a device fabrication process step for harvesting and converting radiant heat (thermal energy) to electricity using nanorectenna arrays. The key application for these devices is waste-heat recovery from cars' exhaust pipes.

1.1 Energy Harvesting

Energy harvesting refers to the conversion of energy from the environment that would have been otherwise lost, into a different form of energy that can be readily utilised (for example electrical energy). Energy harvesting devices can thus enable an increase in efficiency in both industrial and domestic systems as well as underpin new technology [1].

In its essence an Energy Harvesting System (EHS) comprises of an energy source, a conversion device, which performs the actual harvesting and energy conversion, and an energy storage module. The major advantages of an EHS are:

- Free energy source
- Technically maintenance-free when properly installed in a dust-free environment, and can last for the end-application/user's lifetime
- Environmentally friendly.

1.2 Motivation

Any object radiates heat, which is often just dissipated or wasted to the surrounding environment. A large amount of heat is produced and wasted in everyday domestic and industrial activity, such as cooking (in domestic ovens/cookers), home heating/warming (in boilers), domestic heating and power generation (in micro combined heat and power), transport/movement (in automotive exhaust and engines), light and heavy industrial processes

etc. These activities can thus provide an enormous heat source which can be harnessed and recovered as electrical power.

Thermoelectric devices for converting heat to electricity are already well developed, but apart from being bulky, the issue of difficult-to-dispose toxic material (tellurium) as well as low operational efficiency ≈ 7% [2] has been a major factor limiting their widespread use. More environment-friendly, maintenance-free devices, such as rectennas, is the key motivation and theme of this research work. The rectenna device is of special interest because it does not need to be in contact with the hot object/system to operate. Furthermore their manufacturing process is cost effective and does not require materials with high environmental impact and difficult to be disposed of.

1.2.1 Temperature profile Measurement of an Automobile Engine and Exhaust

The main focus of this work is thermal energy harvesting from automotive systems, such as internal combustion engines and exhaust pipes. The temperature profile of an automobile engine and exhaust is thus necessary to identify the most suitable temperature range at which rectennas have to operate.

These temperature profile was carried out on a Volkswagen 1.9 litres diesel engine (used on Polo models), shown in figure 1.1, with the respective thermal images. The key engine parameters are summarised in table 1.1.

Table 1.1: Key engine parameters for the Volkswagen 1.9 litres diesel engine used.

Engine model	Volkswagen SD1
Displacement	1896cc (1.9litres)
Bore and Stroke	79.5mm and 95.5mm

Cylinders	4
Nominal Power	44kW @3600rpm
Nominal Torque	130Nm @ 2200rpm

The engine was operated at a set speed of 2400 rpm for approximately 26 min. with six different throttle and brake (load) values. The temperature readings were taken using thermocouples (shown by the red arrows in figs.1.1a & c). These were connected to four different locations shown in red, in table 1.2.

Table 1.2: Automobile temperature profile measurement values.

Sample No.	Throttle Setting [%]	Brake Setting [%]	Fuel Quantity Injected [mg/r]	Water Flow [l/min]	Air Inlet Pressure [kPa]	Air Inlet Temp [K]	Coolant Inlet Temp [K]	Coolant Outlet Temp [K]	Exhaust Temp [K]	Engine Speed [rpm]
1	12	12	0.0	0.4	0.32	292.6	284.6	285.6	386.2	1318
2	15	0	4.8	0.3	0.32	292.9	284.4	285.4	403.2	2098
3	20	13	4.8	0.3	0.38	294.4	284.1	285.2	444.2	2370
4	25	27	8.8	0.4	0.41	297	283.6	285	504.2	2458
5	30	37	11.2	0.4	0.41	302.2	283.4	284.8	575.2	2399
6	36	46	14.1	0.3	0.44	308.8	282.6	287.4	651.2	2399

From table 1.2, it can be seen that a temperature of 651.2K was recorded at the exhaust manifold as the engine approached the top set speed of 2400 rpm, though not at full load.

a

b

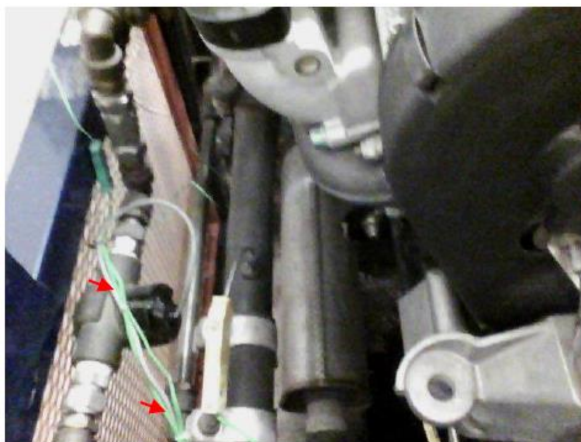

c

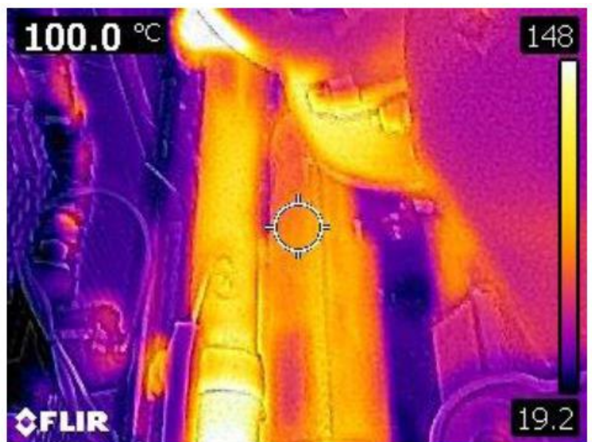

d

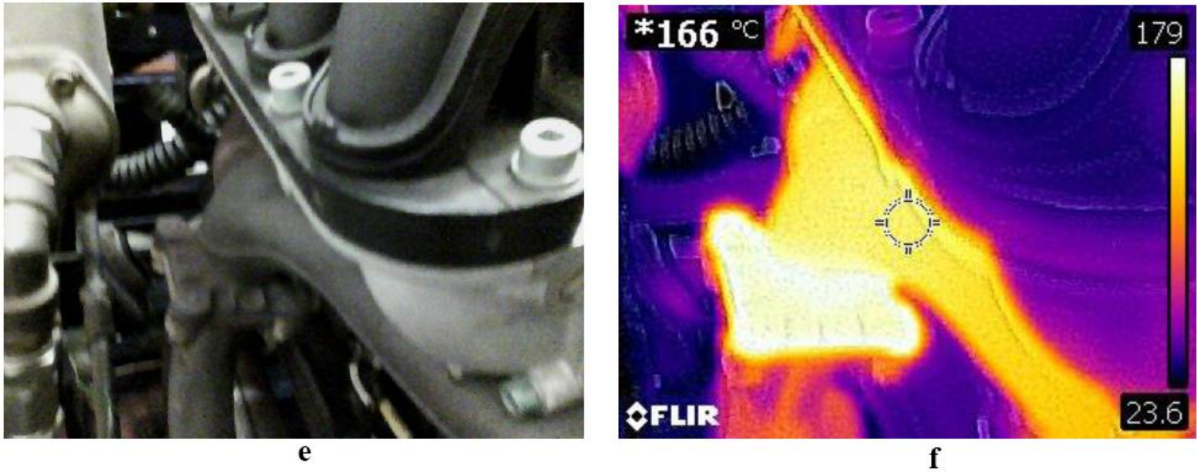

Figure 1.1: Images showing: (a) engine top view, (b) thermal image of the top view, (c) exhaust muffler, (d) thermal image of the exhaust muffler, (e) exhaust manifold and (f) the thermal image of the exhaust manifold. The red arrows are pointing at the green thermocouple wires.

1.3 Thermal Energy

The amount of heat radiated by a body depends on its temperature, with the intensity proportional to the fourth power of the absolute temperature of the body, in accordance with Stefan-Boltzmann's law [3]:

$$E_b = \sigma T^4 \tag{1.1a}$$

where σ is the Stefan–Boltzmann constant and T is the absolute temperature of the body.

Equation 1.1a gives the emissive power of a body for a given temperature over all frequencies. The emissive power as a function of the frequency ν, known as the power spectral density, can be expressed as [4]:

$$E_b = \frac{2h\nu^3}{c^2}\left(\frac{1}{e^{\frac{h\nu}{kT}} - 1}\right) \tag{1.1b}$$

where h is the Planck's constant, c the speed of light in vacuum, and k the Boltzmann's constant.

Thermal radiation has a frequency spectrum that spans from the terahertz region into the near UV region of the electromagnetic spectrum (EMS). The spectrum of this radiation follows the spectral emissive power curves of a black body for different temperatures, and the region is as shown in figure 1.2.

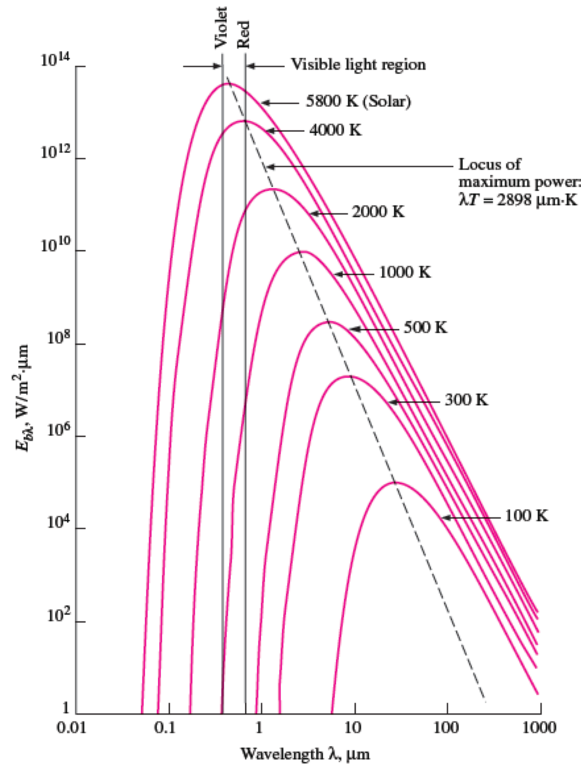

Figure 1.2: Variation of the spectral emissive power of a blackbody with wavelength for different temperatures [4]

Energy harvesting within this region using rectennas is still to a great extent unexplored due to the challenges of technological constraints in fabricating a rectifier that can operate efficiently in this frequency range. Aside from rectennas, other devices that can harvest thermal energy include thermophotovoltaic devices (these also harvest radiant thermal energy) and thermoelectric devices (these harvest non-radiant thermal energy).

1.3.1 Thermophotovoltaic devices:

These devices convert radiant thermal radiation into electricity using photovoltaic cells based on narrow bandgap semiconductors. Filters are typically used to control the spectrum incident

on the Thermo-PV cells [5], [6], [7]. The overall device efficiency, η_{TPV} is the product of the individual efficiencies of the emitter, PV cells and filters.

The main issue with these devices is that radiations with photon energy much higher than the semiconductor bandgap often heats up the photovoltaic cells, thereby endangering the cells. Moreover, filters that can restrict such radiations add a further degree of complexity to the devices.

1.3.2 Thermoelectric devices:

In these devices, temperature gradient and electrical voltage are inter-convertible in accordance with the Seebeck and Peltier effects, which describes how potential difference can be generated by a temperature gradient and how heat flow can be created by the flow of electric current respectively [8] [9]. A simple diagram of the device operation is shown in Fig. 1.3 The device maximum efficiency is dependent on the temperature gradient between the cold and hot ends, in accordance with equation 1.3 [9].

$$\eta_{max} = \frac{T_{hot} - T_{cold}}{T_{hot}} \left(\frac{\sqrt{(1+ZT)} - 1}{\sqrt{(1+ZT)} + \frac{T_{cold}}{T_{hot}}} \right) \tag{1.3}$$

where ZT is the thermoelectric figure of merit given by:

$$ZT = \frac{S_b{}^2 T}{\rho \lambda_{th}} \tag{1.4}$$

where S_b is the Seebeck coefficient, ρ the resistivity, and λ_{th} the thermal conductivity.

Though these devices have the merit of no noise, no vibration or mechanically moving parts, the main challenge is the necessary temperature gradient which requires a cooling system combined with materials, such as tellurium, which is rare, highly toxic, and difficult to dispose.

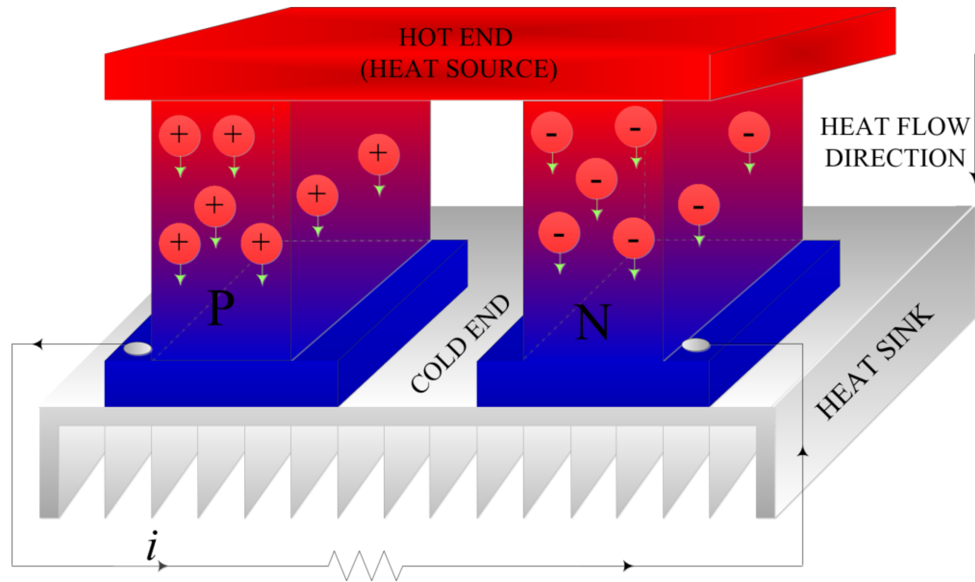

Figure 1.3: A schematic diagram of thermoelectric effect in a thermoelectric device.

A summary of the advantages and disadvantages of the devices discussed is shown in table 1.3.

Table 1.3: Advantages and Disadvantages of the thermophotovoltaic and thermoelectric devices

	Thermophotovoltaic	Thermoelectric
Advantages	• no acoustic noise • no mechanically moving parts, hence no frictional losses	• no acoustic noise • no mechanically moving parts, hence no frictional losses
Disadvantages	• heating up of PV cells by radiations higher than device bandgap • designing filters that can restrict such radiations increases device complexity	• bulky devices • to realize the needed temperature gradient will greatly increase automobile complexity • Tellurium, a rare and toxic material, is one of the major components used in its production
Efficiency	• depends on the individual efficiencies of the PV cells and filters	• depends on the temperature gradient between the cold and hot ends and ZT

1.4 The Rectenna

The word rectenna is coined from rectifying antenna, which means an antenna coupled to a rectifying device. A simple rectenna may consists of a dipole antenna with a rectifier (diode) connected across its feed-point ‘F’ [3], [10] as shown in figure 1.4.

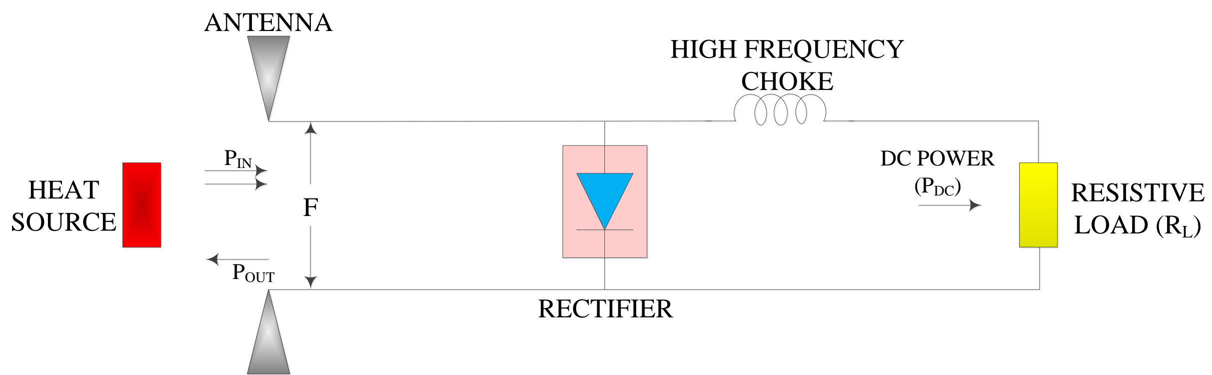

Figure 1.4: A simple rectenna element and heat source [3].

Basic operational principle

The antenna generates a fluctuating signal from the incident radiation. This signal is then converted to DC output by the rectifier and fed to the load R_L through an inductor which prevents (chokes) the radiation from leaking to the load [3].

The features and conditions for optimum performance of a rectenna device include:

i. An antenna that can collect the EM radiation at the desired frequency range.
ii. A high cut-off frequency rectifier with suitable nonlinearity that can convert fluctuating signal to DC.
iii. A good impedance match between the antenna and rectifier.

The antenna considered in this work is a bow-tie antenna. This antenna is considered because it is a broadband antenna, hence it can collect a wide range of frequencies since thermal radiation is a broadband radiation. The schematic of a typical bowtie antenna is shown in figure 1.5, with the rectifier located at feed-point, F [11].

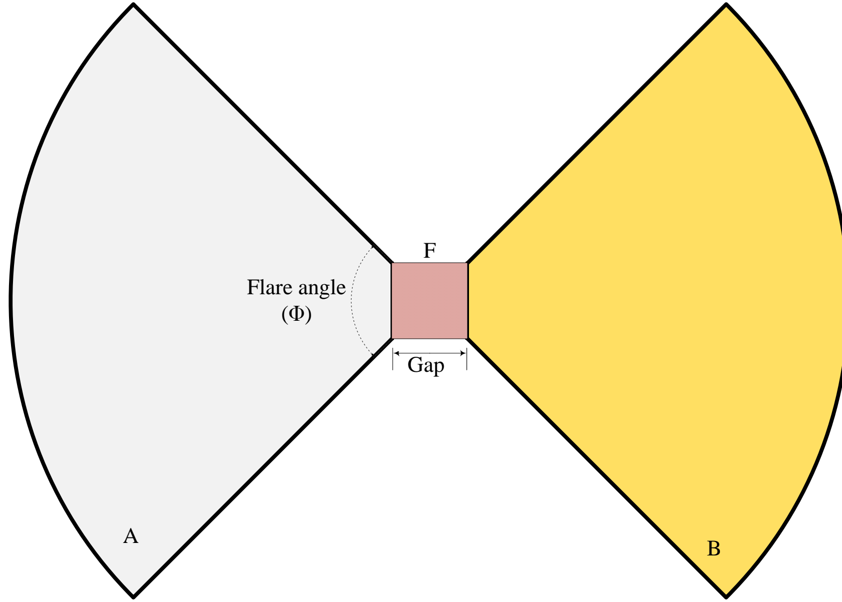

Figure 1.5: A schematic of a typical bowtie antenna.
A and B are the antenna elements (metals of assumed negligible intrinsic resistance), the Gap is the position of the diode, and F is the feed-point [11].

Assuming the heat source and rectifier of the rectenna to be at temperatures T_A and T_D respectively, T_A appears at the antenna feed-point with a Johnson-Nyquist (J-N) power spectral density (PSD), and the maximum power available for conversion from this heat source is expressed as [3], [12]:

$$P_{av} = \frac{\pi^2 k^2}{6h}\left(T_A{}^2 - T_D{}^2\right) \tag{1.5}$$

where k is Boltzmann's constant and h Planck's constant.

It can be seen from (1.5) that the maximum power available for conversion, P_{av}, is proportional to the difference of the squares of the two temperatures T_A and T_D, this is as a result of the nature of the PSD curve shown graphically as the hatched area of figure 1.6.

Since the resonant length of an antenna scales linearly with the wavelength of an incident EM wave [10], and Johnson-Nyquist (J-N) power spectral density (PSD) does not depend on frequency, because thermal noise is white, power according to Eq. 1.5, is not related to the antenna dimension.

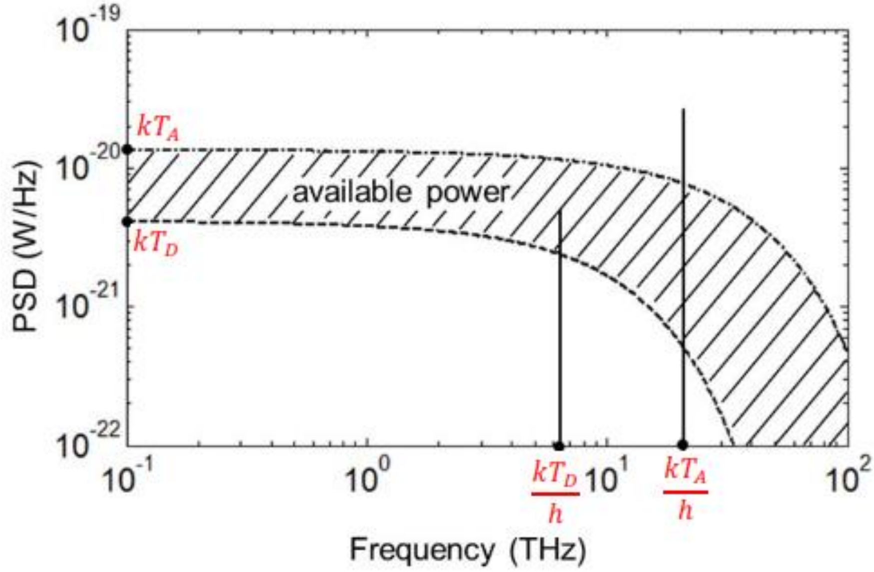

Figure 1.6: PSD curve of the rectenna showing the region of available convertible power [3].

For a given source temperature, the quantum cut-off frequency for maximum power can easily be determined as [3]:

$$f_q = \frac{kT_A}{h} \tag{1.6}$$

In this work, the target operational temperatures are the temperatures obtained from the automobile engine and exhaust profile measurement. Details of the measurement are as already given in section 1.2.1.

The equivalent circuit diagram of the rectenna device is shown in figure 1.7.

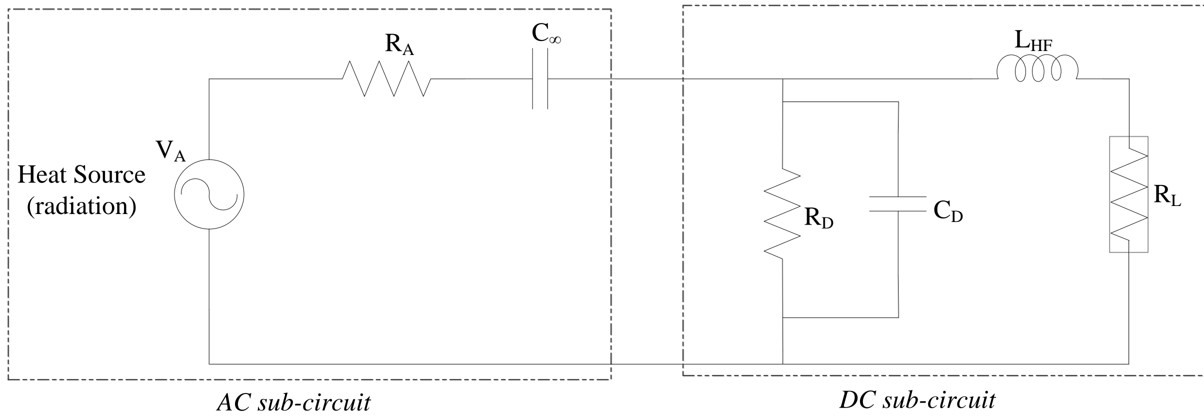

Figure 1.7: An equivalent circuit diagram of the rectenna device.

In the equivalent diagram of figure 1.7, V_A represents the fluctuating source, R_A represents the antenna resistance, C_∞ is a fictitious capacitance which shows the inability of the antenna to radiate a DC signal, R_D represents the diode resistance, C_D represents the diode capacitance, L_{HF} represents the high-frequency inductor serving as choke, and R_L is the resistive load.

Efficient rectenna operation requires matching R_A with R_D (i.e. proper coupling between the antenna and rectifier resistances) and making the time constant, τ, expressed as τ = RC, to be less than the shortest period, T, of the source V_A. Being less than the period, T, makes it possible for signals from the antenna to drop across the diode resistance R_D, rather than being shorted out by the capacitance C_D. This time constant, τ, is used when defining the rectifier cut-off frequency, f_c, which is the upper frequency limit for efficient rectification, above which rectification becomes less efficient [13-15]. The cut-off frequency is expressed as [16]:

$$f_c = \frac{1}{2\pi R_D C_D} \tag{1.7a}$$

where

R_D = diode resistance (differential resistance),

C_D = diode capacitance,

$$C_D = \frac{\varepsilon_o \varepsilon_r A}{d} \tag{1.7b}$$

$$R_D = \frac{1}{A} \times \left. \frac{1}{\left(\dfrac{dJ}{dV_D} \right)} \right|_{V_D = 0} \tag{1.7c}$$

where

A = diode junction area,

d = distance between the two diode metal electrodes; this equally denotes the thickness of the insulating layer,

J = current density through the diode,

V_D = voltage across the diode,

ε_o = vacuum permittivity,

ε_r = relative dielectric constant of the insulating layer.

It can be seen from (1.7a) that the cut-off frequency of the diode depends on its RC time constant. Since efficient device operation requires matching R_A and R_D, the only option left for realizing a high cut-off frequency is to alter the capacitance C_D, expressed as shown in (1.7b). Efficient tunnelling requires that the distance, d, between the two metal electrodes (i.e. thickness of the insulating layer) should be very thin, of the order of 2 to 5nm , this implies that it is only the diode junction area, A, that can be minimized to realize a small time constant.

The overall device efficiency consists of two parts which are radiation and junction efficiencies.

- Radiation efficiency (η_{rad}): This is the efficiency by which the antenna collects and radiates the incident signal/radiation, and it is expressed as [17]:

$$\eta_{rad} = \frac{P_{rad}}{P_{absb}} = \frac{P_{rad}}{P_{rad} + P_{loss}} \tag{1.8}$$

  where P_{rad} , P_{absb} and P_{loss} are the radiated power, power absorbed by the antenna and power dissipated in the material of the antenna, respectively. For P_{rad} to be efficiently coupled to the diode, the impedance of the diode must match that of the antenna to minimize antenna-to-diode power transfer loss.

- Junction efficiency (η_{junc}): This is also known as the tunnelling or rectification efficiency, and is the efficiency by which the diode convert the ac signals to dc. The

junction efficiency is bounded by the Carnot efficiency, which sets a limit to the amount of useable power (work) a heat engine can generate from a thermal source.

1.4.1 Rectenna Dimensions and Temperature Ranges

The resonant length of an antenna scales linearly with the wavelength of the incident EM wave, in accordance with antenna theory [10]. The wavelength at which maximum convertible power can be extracted from the source is determined from the thermodynamic quantum cut-off frequency equation, (1.6), thus:

$$f_q = \frac{kT_A}{h},$$

where c is the speed of light, f_q is the resonant frequency of the antenna, and λ is the wavelength for maximum convertible power, therefore

$$\lambda = \frac{c}{f_q} = \frac{ch}{kT_A} \tag{1.9}$$

Rectenna for Automobile Engine:

The general ambient temperature for normal operation of most automobile engines range between 363.7K and 394.3K [18]. The thermodynamic quantum cut-off frequency and wavelength of this temperature range, is calculated from (1.9) and shown tabulated in table 1.4.

Table 1.4: Quantum cut-off frequency and wavelength of automobile engine.

	Lower value	Upper Value
Temperature (K)	363.7	394.3
Quantum cut-off Frequency (THz)	7.6	8.2
Wavelength (μm)	39.6	36.5

It is worth mentioning here that the higher the temperature of an EM radiation, the shorter the corresponding wavelength, and the more powerful the radiation is as it can easily be deduced from (1.9). The values of the wavelength computed above shows that a micrometre scale rectenna is most suitable for harnessing the thermal radiation of an automobile engine.

Rectenna for Automobile Exhaust:

When an automobile operates with its nominal power at full speed, (i.e. on full load), the temperature of its exhaust ranges between 477.6K and 922K (at the maximum). But working with the temperature profile measurement conducted, the values obtained range from 386.2K to 651.2K. Applying these values to (1.9), gives the respective quantum cut-off frequency and wavelengths as shown tabulated in table 1.5.

Table 1.5: Quantum cut-off frequency and wavelength of automobile exhaust.

	Lower value	Upper Value
Temperature (K)	386.2	651.2
Quantum cut-off Frequency (THz)	8.0	13.6
Wavelength (μm)	37.3	22.1

It can be seen from table 1.5 that micrometre scale rectennas are still very suitable for harnessing the thermal radiation from automobile exhaust.

1.4.2 Rectenna Figures of Merit

Devices are compared using universal figures of merit to bring about technological improvement. Some of the figures of merits that apply to the diode in a rectenna device are:

Differential Resistance (R_D): This is the inverse of the slope of the diode's I-V characteristic. It should be low, (of the order of 100 Ω [19]), to provide good impedance matching between the antenna and the diode. Small barrier height (the difference between the metal work function and insulator electron affinity) and thin insulator are requirements for low R_D.

Responsivity: This is also known as the curvature coefficient, and is a measure of the rectified dc voltage or current with respect to the input power of the incident radiation. It shows how efficiently the diode can rectify signals, and can be calculated directly from the *I–V* characteristics of the diode. The current responsivity (I_{Resp}), defined as the change in dc current per unit power of the absorbed incident radiation, is given by half of the ratio of the second and first derivatives of current with respect to voltage. This is expressed as [20], [21]:

$$I_{Resp} = \frac{1}{2}\left(\frac{d^2I/dV^2}{dI/dV}\right) \quad (1.10a)$$

while the voltage responsivity (V_{Resp}), which is a ratio of the diode's output voltage to the absorbed input power of the incident radiation, is expressed as [5]:

$$V_{Resp} = \left(\frac{V_{out}}{P_{in}}\right) \quad (1.10b)$$

where V_{out} is the output voltage of the diode, and P_{in} is input power of the incident radiation.

The units of current and voltage responsivity are A/W and V/W respectively [5] [20]. A requirement for large responsivity is a large curvature in the I-V curve, this implies a small slope (higher resistance), hence small-barrier height (lower R_D) results to smaller responsivity. To achieve a better responsivity while keeping the resistance low, multi-insulator tunnel diodes could potentially be used [22].

Asymmetry: This is the absolute ratio of forward to reverse bias current at a particular bias voltage. It is related to responsivity which depends on the asymmetrical nature of the I-V curve at a particular bias point, and increases with increasing asymmetry. At zero bias, nonzero responsivity is an indicator of the asymmetry in the I-V curve, which is necessary for rectenna operation. The diode's asymmetry, expressed as shown in (1.11), should be greater than 1 (unity), since a value of 1 indicates full symmetry (i.e. equal barrier heights at both side of the insulator) and hence no rectification [20].

$$F_{Asymmetry} = \left|\frac{J_{forward}}{J_{reverse}}\right| \quad (1.11)$$

where J is current density.

The nonlinearity: This is a ratio of the differential conductance to the conductance, and mathematically, it is double differentiation of the diode current with respect to the voltage. It gives an indication of the sharp turn-on voltage of the diode as well as the extent to which the diode deviates from a linear resistor. The nonlinearity expressed as in (1.12), should be greater than 3 [20] [23].

$$F_{Nonlinearity} = \left(\frac{dJ/dV}{J/V} \right) \tag{1.12}$$

CHAPTER 2

THEORY AND BACKGROUND OF STUDY

Brief discussions of some high frequency (terahertz range) diodes are presented in this chapter, together with some relevant previous research works in the field. A specific terahertz frequency range, 0.75 – 1.1 THz, is considered as it can be conveniently accessed with the equipment available in the THz laboratory in the Engineering Department.

2.1 Rectification

This is the conversion of a fluctuating voltage to a dc voltage using a non-linear device known as a diode. In the context of this work, high frequency diode is implied due to the wavelength and corresponding frequency of the target radiation. High-frequency diodes capable of operating at THz frequencies, include self-switching diodes (SSD), Schottky diodes and metal-insulator-metal (MIM) diodes.

2.1.1 The self-switching diode

An SSD is a planar device fabricated by creating insulating trenches in a semiconductor layer. Applying a positive bias to the device attracts electrons into the channel, thus causing current flow; on the other hand, reversing the bias will repel all the electrons flowing through the channel. These two processes are just the same as forward and reverse bias in a rectifying junction. Although it has a simple architecture with a nonlinear current-voltage (*I*-*V*) characteristic resembling that of a conventional diode, its operational upper frequency limit is within the far infrared region of the EM spectrum [24-26].

2.1.2 The Schottky Diode

The Schottky Barrier Diode (SBD) is a lightly-doped n-type semiconductor-metal junction diode with a typical forward voltage drop in the range of a few hundreds of mV. Their upper frequency limit is still within the far infrared region of the EM spectrum [27-30], [31] and they

require an initial bias for the electrons to overcome the depletion barrier before any significant conduction can occur. It also has a relatively high reverse leakage current.

2.1.3 Metal-insulator-metal (MIM) diodes

The operational principle of these diodes is based on the quantum mechanics principle known as tunnelling. In quantum mechanics, tunnelling means the flow of electrons from the cathode through a thin insulator to the anode, without necessarily acquiring an energy level greater than the energy barrier provided by the insulator. The structure of MIM diodes include a base metal (which acts as the anode), an insulator and a top metal (which acts as the cathode). The insulator can be in the form of an oxide, (then the diode will be properly called a metal-oxide-metal (MOM) diode), or an organic insulator.

MIM diodes are fundamentally fast diodes with operational frequency within the target frequency range of this research work, hence they are the diodes of interest in this work. The point-contact MOM diode has been reported to operate at over 130 THz [32], but it has a major limitation of being structurally unstable due to the fragility of the point of contact (its tip) with the dielectric layer. A major concern about MOM diodes is the oxide dielectric layer. Furnace oxidation of the base metal often results in an oxide of uncontrolled thickness being formed, as well as the formation of a non-uniform layer which are often dominated by pin holes. For tunnelling to occur, the dielectric layer must be very thin (<5 nm thick) [33], and for good throughput, the dielectric layer must equally be very uniform, without pin holes which causes short-circuit, thereby reducing yield. A better and improved method of oxide deposition is the use of a combination of reactive ion-etch and plasma-etch (RIE/PE) oxidation regrowth technique as reported by Dodd et al. [33]. This resulted in a more uniform oxide of controlled thickness being deposited as the dielectric unlike as it was with the furnace oxidation process.

Another challenge of the MOM diode is the presence of tiny pin holes in the oxide layer as well as the possibility of forming other compounds of the actual oxide. To overcome these

challenges, an organic insulator which forms a self-assembled monolayer (SAM) was used as the dielectric layer in place of the metallic oxide [34]. The insulator, octadecyltrichlorosilane, (OTS) has closely packed carbon atoms which form a very uniform monolayer-thick dielectric between the two metal electrodes of the diode. A molecule of the organic insulator consists of a polar head group $SiCl_3$, (of the silane family of compounds), and a long chain methyl-terminated non-polar alkyl-group $C_{18}H_{37}$ as shown in figure 2.1. The polar head attaches firmly to the substrate while the non-polar alkyl tail is held in an upward position to form a monolayer-thick canopy. The dielectric thickness depends on the number of carbon atoms in a chain of the molecule. The thickness of the OTS layer is approximately 2.8nm [35].

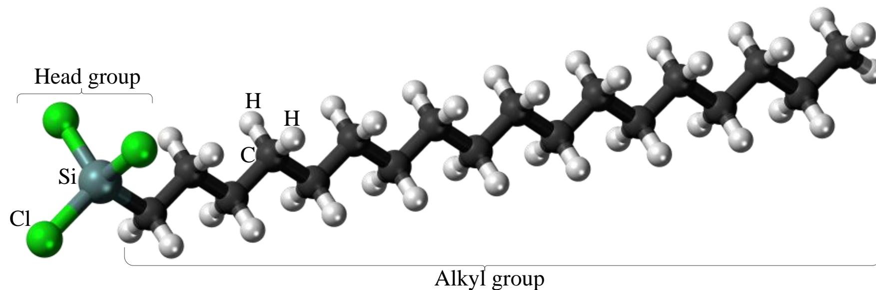

Figure 2.1: A molecule of the organic SAM octadecyltrichlorosilane (OTS).

2.2 Previous Research Works

The concept of exploiting the wave nature of EM radiation and the subsequent conversion to useful electric power via antenna-diode system was originally proposed by R. L. Bailey and J. C. Fletcher during a NASA summer project they undertook in the late 1960s. However, in 1972, R. L. Bailey officially published the concept as a research work where he named the converting device as electromagnetic wave energy converter (EWEC) [36] [37].

A micron-scale metal-oxide-metal diode was developed by Dodd et al. Two dissimilar metals (titanium and platinum), separated by a native oxide (oxide of titanium) produced by reactive ion etching (RIE) and plasma oxidization, were used to realize signal rectification [5]. A stoichiometric analysis of the oxide layer (which comprises of various oxides of titanium) using time of flight secondary ion mass spectrometry (TOFSIMS) reveals that titanium monoxide

(TiO) was the dominant oxide in the layer and not titanium dioxide (TiO_2) as reported in [38]. The major device limitation is that the thickness of the dielectric layer, titanium oxide, was not uniform, this resulted to nonuniform electric field within the device which in addition to impedance mismatch reduced the efficiency greatly. Etor et al. developed a new structure of the MIM diode using a self-assembled organic insulator, in place of the more common metallic oxide. The realized MIM diode which was fabricated had a very uniform insulating layer. This was due to the compactness of the carbon atoms in a molecule of the organic insulator and its self-assembling nature. The device performance was greatly limited because of poor impedance matching. A narrowband matching structure was developed and used with a broadband antenna [34].

Pan et al. demonstrated the conversion of mid and far infrared thermal radiation using a spiral micro antenna and an ultra-fast self-switching diode. The very low efficiency, (0.02%), of their work was still due to a mismatch between the impedance of the diode and antenna structure [3]. Gadalla et al. demonstrated a nanorectenna for infrared detection, using 0.7 nm thick copper oxide (CuO) as an insulator between the overlapping arms of gold and copper. The mismatch between the antenna and diode impedances adversely affected the performance of the device, as there was no structure for impedance matching [39].

Nano antenna dimension, geometric shape and material type are essential factors to consider when determining the electrical properties, absorption and emission capabilities of the antenna. Vandenbosch et al. studied various lengths of dipole nano antennas made of different materials; silver (Ag), gold (Au), aluminium (Al), copper (Cu) and chromium (Cr), with a view to determining the optimum upper boundary absorption and radiation efficiency limit for harvesting solar energy. They stated that Aluminium (Al) which is lesser in total harvesting efficiency (about 50%) and forms a transparent oxide is preferred to the high efficient Silver (Ag), which is prone to oxidization, and Gold (Au) which is very expensive [17]. In a later

development, they analysed the overall efficiency of the nanorectenna by considering the efficiencies of the two phases involved in its operation i.e. EM radiation absorption efficiency and rectification efficiency, and proposed that for a match between the impedance of the antenna and the rectifier, the rectifier impedance should be of the order of 100 Ω [19] [13].

Periasamy et al. developed a point-contact MIM diode structure, using anodic oxidation (of the metal layer) for insulator deposition. In contrast to the complete conventional planar structure, the second metal is in the form of a bent wire and hence results in a point-contact diode area. The point contact approach drastically reduces the diode contact area, which consequently reduces the capacitance and RC constant, thus helping to achieve a reasonably high cut-off frequency. Although this method proves to be very useful when studying the effect of metal work-function difference on the electrical properties of MIM diodes [40 - 43] [16], the delicate nature of the point of contact (tip) makes the device to be fragile and structurally unstable.

Krishnan et al. fabricated MIM tunnel diodes for IR-detectors operating at room temperature and used them to experimentally determine the effect of dielectric thickness and contact area on the I-V characteristics of the diodes. The outcome of their work was a confirmation that decreasing both the insulator thickness and diode contact area increases tunnelling current [44]. A graphene-semiconductor rectenna in which the bowtie antenna is a monolayer graphene while an n-type Gallium Arsenide (n-GaAs) semiconductor serves as the substrate was proposed by Dragoman et al. The device has a very poor nonlinearity, in addition to the fact that the performance was limited by the formation of a Schottky barrier at the graphene-semiconductor interface [45].

With a carbon nanotube-based optical rectenna, Anderson et al. were able to demonstrate rectification within the wavelength range of 404nm to 980nm, with maximum rectification at a wavelength of 638nm. The very low efficiency,$3 \times 10^{-6}\%$, of the device was due to the thick

dielectric layer, (a 16 nm quad-insulator stack of $Al_2O_3/ZrO_2/Al_2O_3/ZrO_2$), which resulted to a large device resistance [46]. Cowell et al used ZrCuAlNi thin film electrode to fabricate both symmetrical and asymmetrical MOM diodes with Al_2O_3 as the dielectric layer. ZrCuAlNi (in the ratio of 40:35:15:10) formed the two electrodes for the symmetrical diode while Aluminium was the upper electrode for the asymmetrical diode. Impedance mismatch in addition to a defective dielectric layer caused by the formation of a native oxide ZrO_2 before the actual Al_2O_3 are the major limitations of the device [47].

Auton et al. used a small area local gate to optimize a graphene ballistic rectifier (GBR) integrated with a broadband antenna. The device which has a very high impedance, 6.7 MΩ at zero bias, was used demonstrate terahertz (THZ) imaging at a reported frequency of 685 GHz. The high device impedance at zero bias was a big mismatch to the antenna impedance of approximately100 Ω, as there was no structure for matching the impedances [48].

Balocco et al. designed and fabricated an array of nanowires with broken symmetry, otherwise known as self-switching diodes (SSDs), and were able to detect microwaves up to 110 GHz at room temperature with the diodes. At a bias current of 10 µA, the impedance of the 18 parallel nanowires was approximately 50 kΩ; this was a significant mismatch to the 50 Ω RF source since an estimated 0.4% of the RF input power was effectively utilized by the device while about 99.6% was reflected, this thus adversely affected the device performance. In a later development, they experimented on the SSDs using a free electron laser at temperatures less than 150 K, and were able to detect signals at 2.5 THz [49, 50]. By coupling the SSDs to a self-complementary 200 nm thick Au bowtie micro-antenna, Balocco et al were able to achieve signal rectification at room temperature up to 1.5 THz. However, the mismatch between the antenna impedance of 72 Ω and the SSD impedance of 150 kΩ adversely affected power transfer which thus limited the device performance [25]

Although conventional rectification at RF and microwave frequencies has made possible the development of micro rectennas with conversion efficiencies as high as 91%, due to great improvement in the efficiency of the rectifying diodes [51], the development of real time infrared and optical frequency rectenna is still a very big challenge [52].

A summary of the previous relevant research works reviewed with their respective limitations is shown in table 2.1.

Table 2.1: A summary of some previous relevant research works with their limitations.

Authors	**Type of Device**	**Detected Frequency**	**Efficiency**	**Limitation**
Dodd et al, 2014	Metal-Oxide-Metal Diode (MOM)	Not Available	Not Available	Nonuniform thickness of the dielectric layer, Titanium oxide, results to nonuniform electric field which reduced yield greatly
Etor et al, 2016	Metal-Insulator-Metal Diode (MIM)	20GHz	Not Available	Developed impedance matching structure is narrowband while antenna is broadband; this thus limited power transfer.
Pan et al, 2014	Spiral antenna & SSD (Self-switching Diode)	5.3THz	0.02%	Impedance mismatch b/w antenna and diode greatly affected yield
Gadalla et al, 2014	Metal-Oxide-Metal Diode (MOM)	28.3THz	Not Available	No structure for matching the impedance. Variation in diode and antenna impedance affected device efficiency greatly.
Periasamy et al, 2010	Point-contact Junction	Not Available	Not Available	Very fragile and delicate point-contact
Krishnan et al, 2008	Metal-Oxide-Metal Diode (MOM)	Not Available	Not Available	Nonuniform thickness of the dielectric Nickel oxide (NiO) results to nonuniform electric field which reduced yield greatly

Dragoman et al, 2016	Graphene/n-GaAs rectenna	897GHz	Not Available	The formation of a Schottky barrier at the graphene-semiconductor interface limits the maximum frequency to GHz; device nonlinearity is very poor.
Cowell et al, 2011	Metal-Oxide-Metal Diode (MOM)	Not Available	Not Available	Defect in dielectric layer due to the formation of a native oxide ZrO_2 before the actual Al_2O_3 in addition to impedance mismatch
Anderson et al, 2019	Carbon nanotube Rec.	Optical (4.7×10^{14}Hz)	3×10^{-6}%	The very thick dielectric layer, 16nm, resulted to large device resistance, hence low efficiency
Auton et al, 2017	Graphene Ballistic Rectifiers for THz detection and imaging	685GHz	Not Available	High device impedance at zero bias was a big mismatch to antenna impedance
Balocco et al, 2005	SSD (Self-switching Diode)	110GHz	Not Available	High device impedance reduced efficiency drastically
Balocco et al, 2008	SSD at a temp. < 150 K	2.5THZ	Not Available	High device impedance reduced efficiency drastically
Balocco et al, 2011	SSD at room temp. 300 K	1.5THZ	Not Available	High device impedance reduced efficiency drastically

CHAPTER 3

CONDUCTION MECHANISMS AND NUMERICAL SIMULATION

This chapter covers the current conduction mechanisms occurring in a MIM diode, which is the diode of interest in this research work and the key component of the considered rectennas.

3.1 Conduction Mechanisms within a Metal-Insulator-Metal Diode

Various types of current conduction mechanisms occur through a thin dielectric film (an insulator) sandwiched between the two metal electrodes of an MIM diode, and these are as a result of the interaction between the electrodes and the insulator. They include: direct electron tunnelling, Fowler-Nordheim (F-N) tunnelling, Schottky emission, Poole-Frenkel (P-F) emission and hopping conduction.

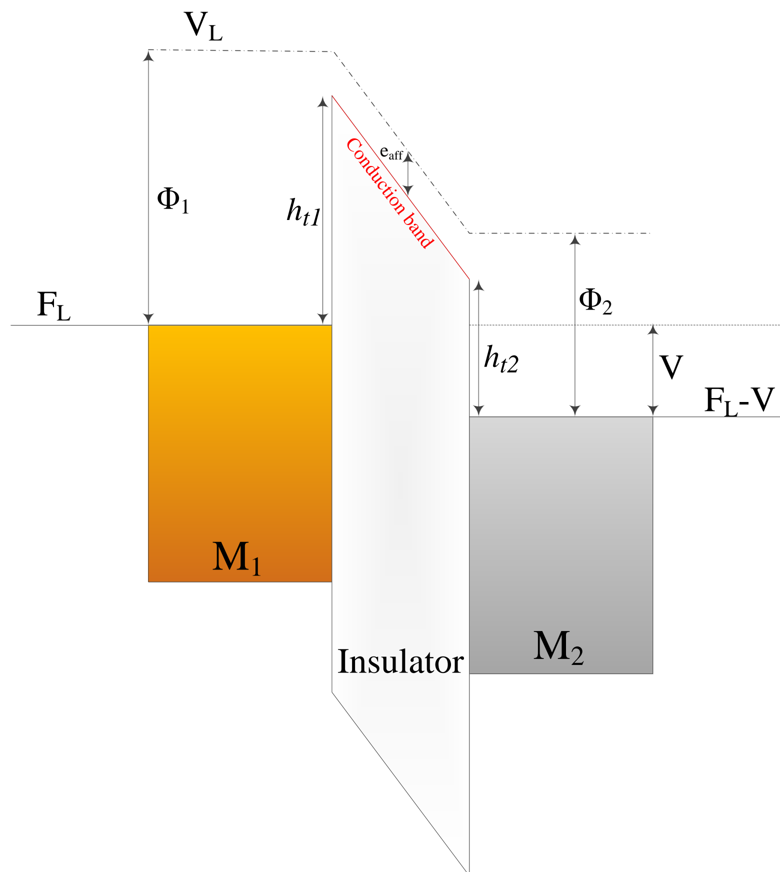

Figure 3.1: Schematic energy band diagram of an MIM diode showing its biased state with an applied positive voltage V on M_2.

In the energy band diagram of figure 3.1, V_L is the vacuum level (energy level of electrons that are outside the material), F_L is the Fermi level (energy level above which all states are empty and below which all states are filled up at absolute zero), e_{aff} is the electron affinity of the insulator, Φ_1 is work function of metal 1 (M_1 is cathode), while Φ_2 is work function of metal 2 (M_2 is anode); h_{t1} and h_{t2} are the barrier heights at M_1-insulator and M_2-insulator junctions respectively.

According to classical physics, an electron can only overcome and crossover a potential barrier when its energy level is greater than that of the potential barrier. However, in quantum mechanics the wave nature of electron makes it possible for an electron to pass through (tunnel through) a barrier into the dielectric layer without necessarily acquiring an energy level greater than that of the potential barrier. When the electrodes of an MIM diode are polarized, an electric field develops across the dielectric layer which must be very thin (<5 nm thick) for tunnelling to occur.

3.1.1 Direct Electron Tunnelling

When the dielectric thickness is less than 3.5 nm, direct electron tunnelling becomes the dominant tunnelling mechanism [53]. In direct tunnelling unlike the F-N tunnelling, electrons tunnel through the barrier, directly across the dielectric layer, into the anode electrode as shown in the energy band diagram of figure 3.2. The current density for direct electron tunnelling is expressed as [53-57]:

$$J = N\,exp\left\{\frac{-8\pi\left(\sqrt{\left(2m_T{}^{*}\right)}\right)}{3hqE}\left(h_t\right)^{\frac{3}{2}}\left[1-\left(1-\frac{V}{h_t}\right)^{\frac{3}{2}}\right]\right\} \qquad (3.1a)$$

$$N = \frac{Cq^2}{8\pi h\varepsilon_o\varepsilon_r h_t} \qquad (3.1b)$$

where V is the applied voltage, C is a correction factor which is a function of the applied voltage, barrier height, and the dielectric thickness, q is the electron charge, h is the Planck's constant, h_t is the barrier height, ε_o is the permittivity of free space, ε_r is the insulator dielectric constant, m_T^* is the effective mass of the electrons in the dielectric, and E is the electric field in the dielectric (assumed constant).

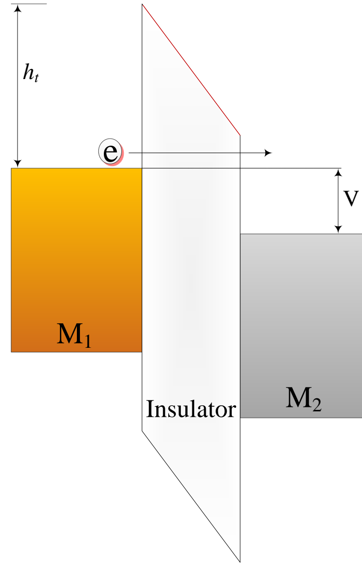

Figure 3.2: Schematic energy band diagram of an MIM diode showing Direct tunnelling.

3.1.2 Fowler-Nordheim (F-N) Tunnelling

In F-N tunnelling, the electric field across the dielectric is high enough to make the energy barrier thinner than at zero bias [53]. In this tunnelling mechanism, electrons tunnel through the potential barrier into the conduction band of the dielectric as shown in figure 3.3. The density of the tunnelling current under this mechanism is expressed as [53-56]:

$$J = \frac{q^3 E^2}{8\pi h h_t} exp\left[\frac{-8\pi\left(\sqrt{\left(2qm_T^*\right)}\right)}{3hE}(h_t)^{\frac{3}{2}}\right] \tag{3.2}$$

where m_T^* is the effective mass of electrons in the dielectric, h is the Planck's constant, q is the electron charge, E is the electric field across dielectric, and h_t is barrier height.

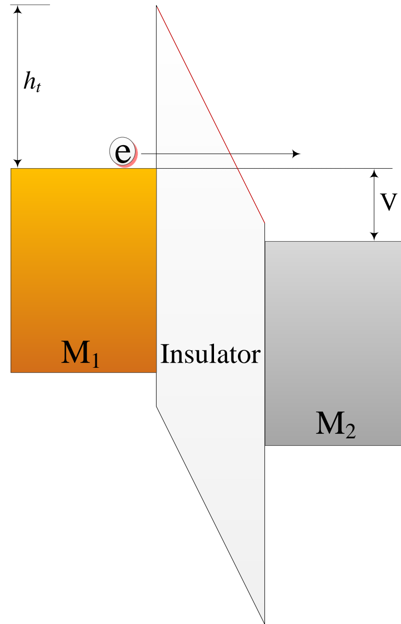

Figure 3.3: Schematic energy band diagram of an MIM diode showing F-N tunnelling.

3.1.3 Schottky emission

This is also known as thermionic emission, and it is the process of emitting thermally excited electrons, with sufficient energy, from the surface of a metal to overcome the potential energy barrier at a metal-dielectric or metal-semiconductor interface. The height of the potential barrier can be lowered by the image force which is best described as the electrostatic force on a charge near a conductor. The image force is a force of attraction as a result of the electric image of the charge, and the barrier-lowering effect of image force is known as Schottky effect [53]. Schottky emission is the most common current conduction mechanism in a dielectric at relatively high temperatures.

The current density, J of majority carriers in an M-S junction under thermionic emission is expressed as [53-56]:

$$J = A^{*}T^{2}\, exp\left[\frac{-q\left(h_t - \sqrt{\dfrac{qE}{4\pi\varepsilon_o\varepsilon_r}}\right)}{kT}\right] \quad (3.3a)$$

$$A^* = \frac{4\pi qk^2 m^*}{h^3} \tag{3.3b}$$

where A^* is Richardson constant, E is the electric field across dielectric, T is the absolute temperature, q is the electron charge, h_t is the barrier height, h is the Planck's constant, m^* is the electron mass in dielectric, k is the Boltzmann's constant, ε_o is the permittivity of free space, and ε_r is the dynamic dielectric constant.

The energy band diagram depicting Schottky emission in a metal-insulator-metal diode is shown in figure 3.4.

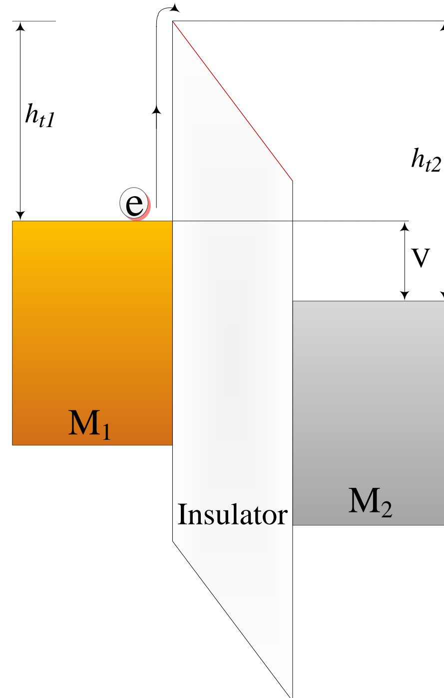

Figure 3.4: Schematic energy band diagram of an MIM diode showing Schottky emission.

3.1.4 Poole-Frenkel (P-F.) Emission

This is also known as internal Schottky emission, and entails the emission of electrons from traps within the dielectric into the conduction band of the dielectric as a result of thermal excitation, as shown in figure 3.5. Traps may result from oxygen vacancies in oxide dielectric when an electric field is applied at a high temperature [53].

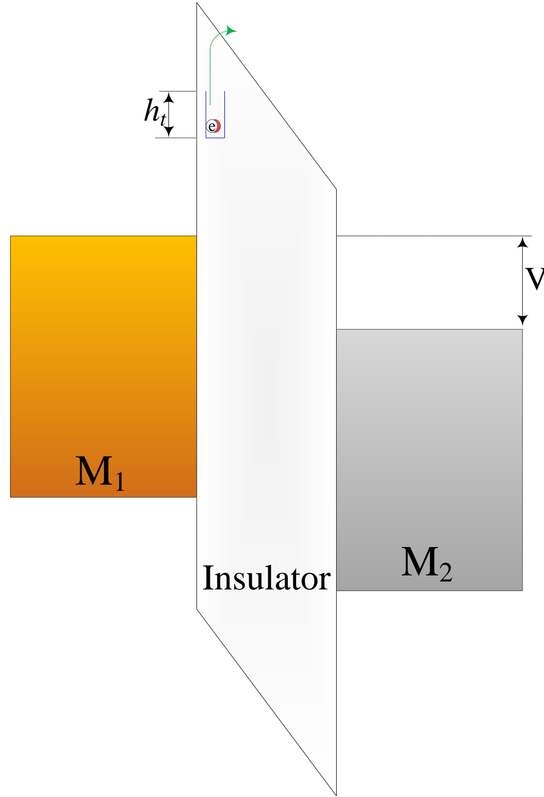

Figure 3.5: Schematic energy band diagram of an MIM diode showing P-F emission.

The barrier height in P-F emission is the depth of the potential well where the electron is trapped. Applying an electric field across the dielectric reduces the potential energy of the trapped electron, thereby increasing the probability of its being thermally excited out of the trap; this means that P-F emission normally occurs when an electric field is applied at a high temperature. The density of current flow as a result of this conduction mechanism is expressed as [53-56]:

$$J = P^* exp\left[\frac{-q\left(h_t - \sqrt{qE/\pi\varepsilon_o\varepsilon_r}\right)}{kT}\right] \tag{3.4}$$

where P^* is a constant, other notations are as already defined.

3.1.5 Hopping Conduction

This is a non-thermally activated process, and entails the tunnelling of electrons from one trap site to another within the dielectric film. If the trap sites are of the same energy level, an elastic tunnelling is said to occur. Conversely, when tunnelling is between trap sites of varying energy

levels, inelastic tunnelling occurs. Energy band diagram of an MIM diode showing the hopping conduction mechanism is shown as *e* and *f* in figure 3.6.

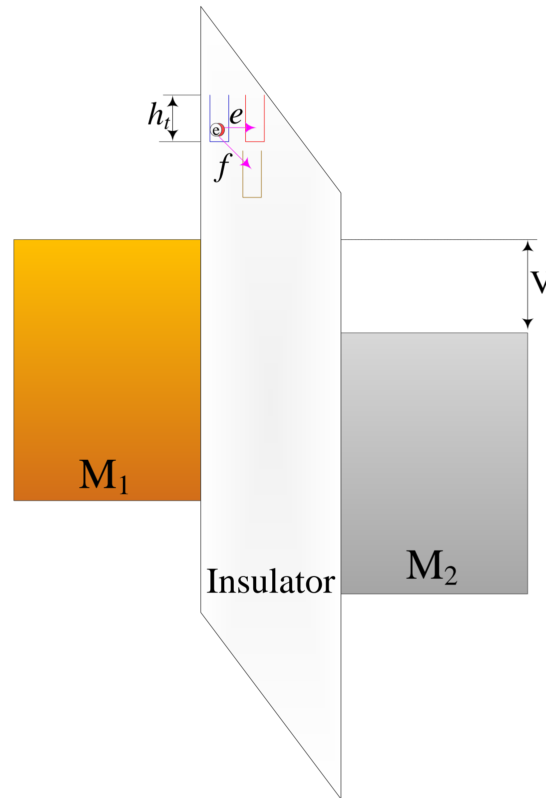

Figure 3.6: Schematic energy band diagram of an MIM diode showing (e) Elastic and (f) Inelastic Hopping tunnelling respectively.

The current density of electrons hopping from one trap site to another in a dielectric film can be expressed as [5] [53-56]:

$$J = q\left\{a(nv)exp\left[\frac{qaE - E_a}{kT}\right]\right\} \tag{3.5}$$

where q is the electron charge, a is the mean spacing between trap sites, n is the concentration of electrons in the dielectric conduction band, v is the vibration frequency of electrons within the traps, E is the electric field across dielectric, E_a is the activation energy from trap site to the minimum level of the conduction band; other notations are as already defined.

Device operation is not determined by any single conduction mechanism, rather there is always a combination of different mechanisms which can occur simultaneously or at different times during the operation of the device depending on the operational voltage, temperature, and dielectric thickness.

As mentioned before, the structure of an MIM diode includes a base metal (which acts as the anode), an insulator and a top metal (which acts as the cathode). In this research work, Titanium (Ti) and Platinum (Pt) with work functions 4.33eV and 5.65eV, respectively, are considered as the base metal (M_2) and top metal (M_1).

Metal electrodes with dissimilar work function are normally used because they induce built-in voltage (V_{bi}) across the insulator when the device is under thermal equilibrium. This built-in voltage is the potential barrier which electrons must overcome, when the device is biased, before any form of current conduction can take place. If V_{bi} is zero, the MIM structure will be ohmic and there will be no rectification; it is thus necessary to maximize the work function difference. Narrow bandgap (high electron affinity) materials should be considered and used as insulators since they give rise to small barrier height which is a requirement for both low resistance and low turn-on voltage (V_{on}) [58].

3.2 Numerical Simulation of Charge Transport across the Dielectric Layer

A good knowledge of the quantum transmission probability of charge carriers through an ultra-thin dielectric layer is required for the modelling and numerical simulation of tunnelling current.

Some attempts to make the calculation of tunnelling currents through thin dielectric layers easier followed the ground-breaking work of Fowler and Nordheim [59, 60]. Gundlach et al [61] were able to prove that oscillations occur in the tunnelling I-V curves using the transmission probability of a trapezoidal barrier. Maserjian et al [62] in their work

experimentally observed these oscillations from F-N currents tunnelling through thermally grown SiO_2 insulating layer of thickness less than 4 nm.

The theoretical study, at low voltages ($V \approx 0$) and high voltages ($V > \frac{h_t}{q}$), of the tunnelling effect of current between two metal electrodes separated by a sufficiently thin insulating layer was first made by Sommerfeld and Bethe [63]. Holm extended the theory to intermediate voltages ($0 < V \leq \frac{h_t}{q}$) [64-66], while J. G Simmons derived a generalised theory for this tunnelling effect which makes possible the derivation of more accurate expressions as well as the resolution of the inconsistencies associated with the works of Sommerfeld, Bethe and Holm [65]. These earlier works of Sommerfeld and Bethe, Holm, and Simmons all concentrated on similar metallic electrodes, having the same work function, in which case the polarity of the applied voltage has no effect on the I-V characteristic of the tunnelling junction.

In a later work, J. G. Simmons extended the theory to include dissimilar metallic electrodes with dissimilar work functions [66]. When dissimilar electrodes are used, the nature of the I-V characteristic of the tunnelling junction depends on the polarity of the applied voltage. At low voltages, the tunnelling junction becomes forward biased when the electrode with lower work function is positively biased; however, at a higher voltage the junction becomes forward biased when the electrode with higher work function is positively biased.

Under thermal equilibrium, a potential barrier develops in a dielectric layer separating the two metallic electrodes of a metal insulator metal tunnel junction. If the junction is composed of similar electrodes, then the barrier is said to be symmetrical; if on the other and the junction is made up of dissimilar electrodes, an asymmetrical barrier builds up within the dielectric layer. This asymmetric barrier is caused by an intrinsic field, F_{int}, which develops within the dielectric

layer due to the contact potential difference between the two electrodes whose work functions differ.

The intrinsic field, F_{int}, is expressed as:

$$F_{int} = \frac{\Phi_1 - \Phi_2}{qd} \tag{3.6}$$

where Φ_1 and Φ_2 are the work functions of the first and second electrodes, q is the electron charge, and d is the thickness of the dielectric layer.

As discussed earlier, an asymmetric potential barrier develops within the dielectric layer of an asymmetric metal insulator metal diode. The barrier being asymmetric simply means that the barrier heights are not equal, hence $\Delta h_t \neq 0$. The fact that $\Delta h_t \neq 0$, was not considered in the conventional F-N tunnelling theory which describes the emission current as [59]:

$$I = \frac{AV^2}{dh_t} exp\left(\frac{-Bdh_t^{\frac{3}{2}}}{V}\right) \tag{3.7}$$

where A and B are constants, V is the applied voltage, d is the thickness of the barrier, and h_t is the barrier height.

This not only compromises the accuracy when determining the F-N tunnelling current of an asymmetrical MIM tunnelling junction, but also affects the accuracy when estimating the barrier height. From (3.7), Millikan et al [67] first described the linearity of plotting $log\left(\left|\frac{I}{V^2}\right|\right)$ versus $\frac{1}{V}$, which otherwise is known as the Fowler-Nordheim (F-N) plot.

3.2.1 Estimation of the barrier heights of an asymmetric MIM tunnel junction

The accuracy of estimating the barrier heights of an asymmetrical MIM tunnelling junction is greatly improved when the difference in barrier height is considered and not neglected, i.e. $\Delta h_t \neq 0$. Incorporating the difference in barrier height component, Δh_t, into (3.7) results to an emission current expression given as [68], [53, 54]:

$$I = \frac{A(V + \Delta h_t)^2}{dh_t} exp\left(\frac{-Bdh_t^{\frac{3}{2}}}{V + \Delta h_t} \right) \tag{3.8}$$

where $\Delta h_t = h_{t1} - h_{t2}$ is the difference in barrier height, all other notations are as already defined.

From (3.8), a plot of $log\left(\left| \frac{I}{(V + \Delta h_t)^2} \right| \right)$ versus $\left| \frac{1}{(V + \Delta h_t)} \right|$, which is more accurate than the conventional F-N plot of $log\left(\left| \frac{I}{V^2} \right| \right)$ versus $\frac{1}{V}$, for an asymmetrical MIM tunnelling junction can be made. By fitting this plot to the current-voltage (I-V) experimental data of an asymmetrical MIM tunnelling junction, the barrier heights h_{t1} and h_{t2} can be estimated as fitting parameters. This underscores the importance of Δh_t, as the source of asymmetry in an asymmetrical MIM tunnelling diode.

Figure 3.7 is the schematic energy band diagrams of a biased MIM tunnelling diode showing (a) forward biased and (b) reverse biased conditions respectively. When the diode is forward biased, by applying a positive voltage to the lower work function electrode, the magnitude of the current tunnelling through the junction is expressed as [68], [53, 54]:

$$I^+ = \frac{K_1}{h_{t1}} (V + \Delta h_t)^2 \; exp\left(-K_2 (h_{t1})^{\frac{3}{2}} \frac{1}{V + \Delta h_t} \right) \tag{3.9}$$

where the constant K_1 is a function of the dielectric thickness and tunnelling junction area, while K_2 is a function of the effective mass of tunnelling electrons in the dielectric as well as the dielectric thickness; all other notations are as already defined.

Evaluating (3.9) further results to the tunnelling current density equation already expressed in (3.2) [53, 54].

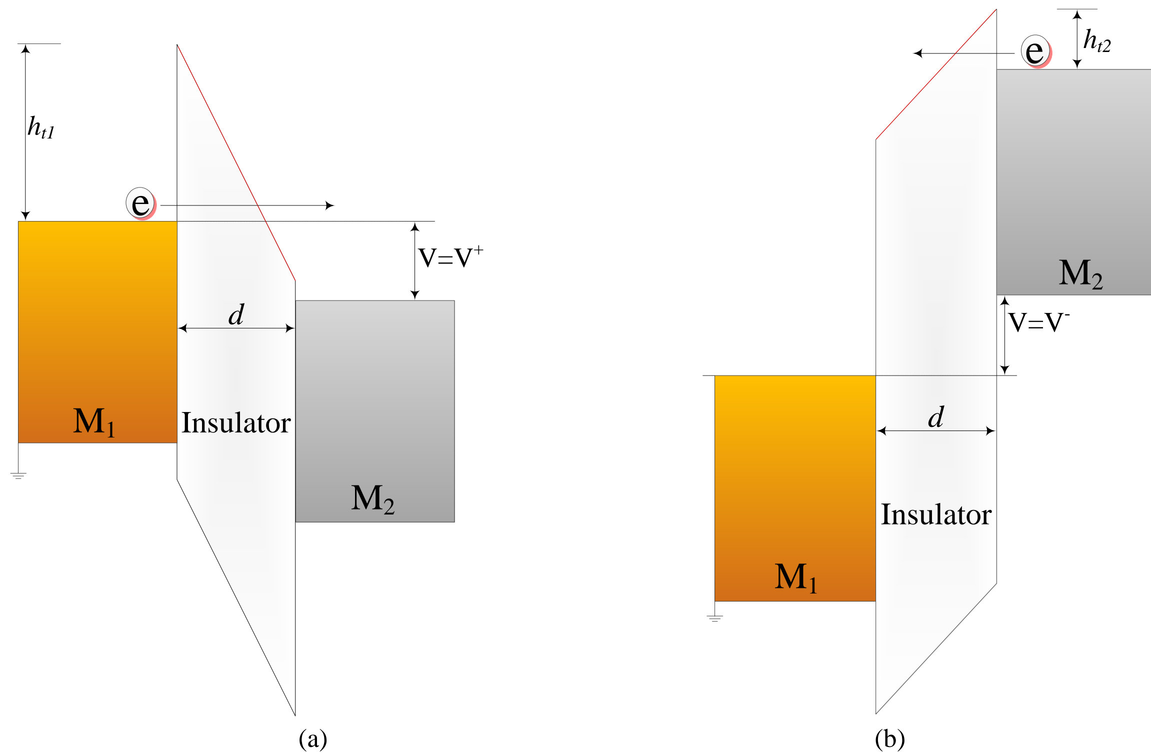

Figure 3.7: Schematic energy band diagrams of a biased MIM tunnelling diode showing (a) forward biased and (b) reverse biased conditions; M_2 is lower work function electrode.

Similarly, when reverse biased, the same magnitude of current tunnels through the junction, with the only difference being the change in sign as shown in (3.10).

$$I^{-} = -\frac{K_1}{h_{t2}}(V+\Delta h_t)^2 \, exp\left(-K_2(h_{t2})^{\frac{3}{2}}\frac{1}{V+\Delta h_t}\right) \tag{3.10}$$

It can be seen from (3.9) and (3.10) that the current tunnelling through the MIM junction for either of the two bias conditions depends on the two barrier heights. It is the need for proper estimation of the barrier heights when modelling the charge transport (tunnelling current) across the dielectric layer of a metal insulator metal junction. It is worth mentioning that F-N

tunnelling only becomes the dominant conduction mechanism within the diode when the applied voltage bias is greater than the barrier heights, h_{t1} and h_{t2}, for either the forward or reverse bias conditions respectively.

For a proper analysis of an asymmetrical MIM tunnelling diode, (3.9) and (3.10) are linearized as [68], [53, 54]:

$$log\left(\frac{I^{+}}{(V+\Delta h_t)^2}\right) = log\left(\frac{K_1}{h_{t1}}\right) - \left(\frac{K_2 (h_{t1})^{\frac{3}{2}}}{2.3}\right)\frac{1}{V+\Delta h_t} \tag{3.11}$$

$$log\left(\left|\frac{I^{-}}{(V+\Delta h_t)^2}\right|\right) = log\left(\frac{K_1}{h_{t2}}\right) - \left(\frac{K_2 (h_{t2})^{\frac{3}{2}}}{2.3}\right)\frac{1}{V+\Delta h_t} \tag{3.12}$$

The linearity of the characteristic plot of $log\left(\left|\frac{I}{(V+\Delta h_t)^2}\right|\right)$ versus $\left|\frac{1}{(V+\Delta h_t)}\right|$ is very evident from equations (3.11) and (3.12). The magnitude of the slope and intercept of the characteristic plot for the forward and reverse bias conditions can easily be deduced from (3.11) and (3.12) as:

$$m^{+} = \left(\frac{-K_2 (h_{t1})^{\frac{3}{2}}}{2.3}\right) \tag{3.13}$$

$$m^{-} = \left(\frac{K_2 (h_{t2})^{\frac{3}{2}}}{2.3}\right) \tag{3.14}$$

$$b^{+} = log\left(\frac{K_1}{h_{t1}}\right) \tag{3.15}$$

$$b^{-} = log\left(\frac{K_1}{h_{t2}}\right) \tag{3.16}$$

where m^+ and m^- are the slopes of the characteristic plots for the forward and reverse bias conditions respectively, while b^+ and b^- are the intercepts of the characteristic plots for the forward and reverse bias conditions respectively.

Equations (3.13) and (3.14) are the expressions for the forward and reverse bias slope while (3.15) and (3.16) are the expressions for the forward and reverse bias intercept.

Considering the ratio of the forward and reverse bias barrier heights from the slope and intercept expressions gives:

$$\left|\frac{m^+}{m^-}\right| = \left(\frac{h_{t1}}{h_{t2}}\right) = r \tag{3.17}$$

$$10^{b^- - b^+} = \left(\frac{h_{t1}}{h_{t2}}\right) = r \tag{3.18}$$

Given the fact that $\Delta h_t = h_{t1} - h_{t2}$, the barrier heights h_{t1} and h_{t2} can therefore be estimated correctly from (3.17) and (3.18) as:

$$h_{t1} = \left(\frac{r\Delta h_t}{r-1}\right) \tag{3.19}$$

$$h_{t2} = \left(\frac{\Delta h_t}{r-1}\right) \tag{3.20}$$

The experimental data of four asymmetrical MIM diodes fabricated using dielectric layers of different self-assembled monolayers (SAMs) having different chain lengths are shown in table 3.1. These data were used in validating the accuracy of barrier height estimation as suggested by Simmons.

Table 3.1: Experimental data of some fabricated asymmetrical MIM diodes [69]

SAM (dielectric layer)	s (nm) dielectric thickness	Δh_t (eV)	h_{t1} (eV)	h_{t2} (eV)
C8	1.2	0.084	0.263	0.179
C10	1.34	0.1	0.287	0.187
C12	1.57	0.157	0.422	0.265
C18	2.23	0.373	0.448	0.075

In order to validate the data shown in table 3.1, the I-V characteristics of the fabricated MIM junctions were numerically simulated and plotted in matlab, using a custom code already available in the group. The code is based on the non-equilibrium Green function (NEGF) approach proposed by Datta for the simulation of nano and molecular devices [70]. The plots are as shown in figure 3.8.

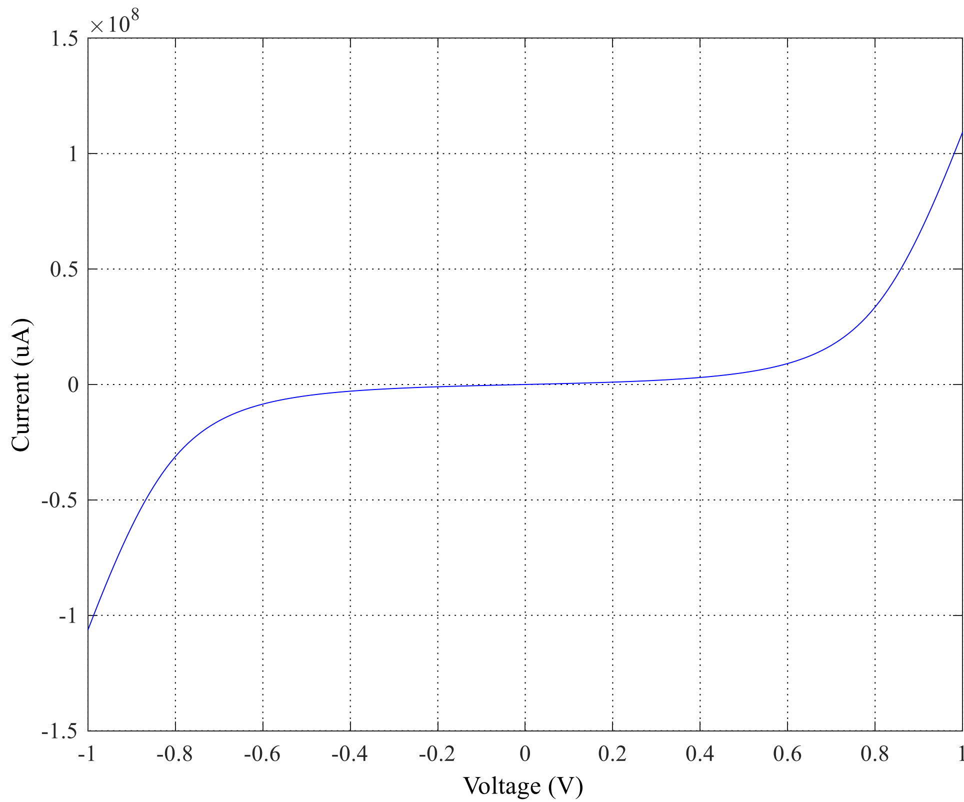

(a) I-V characteristic curve of 100µm^2 MIM diode with 8-Carbon atom SAM

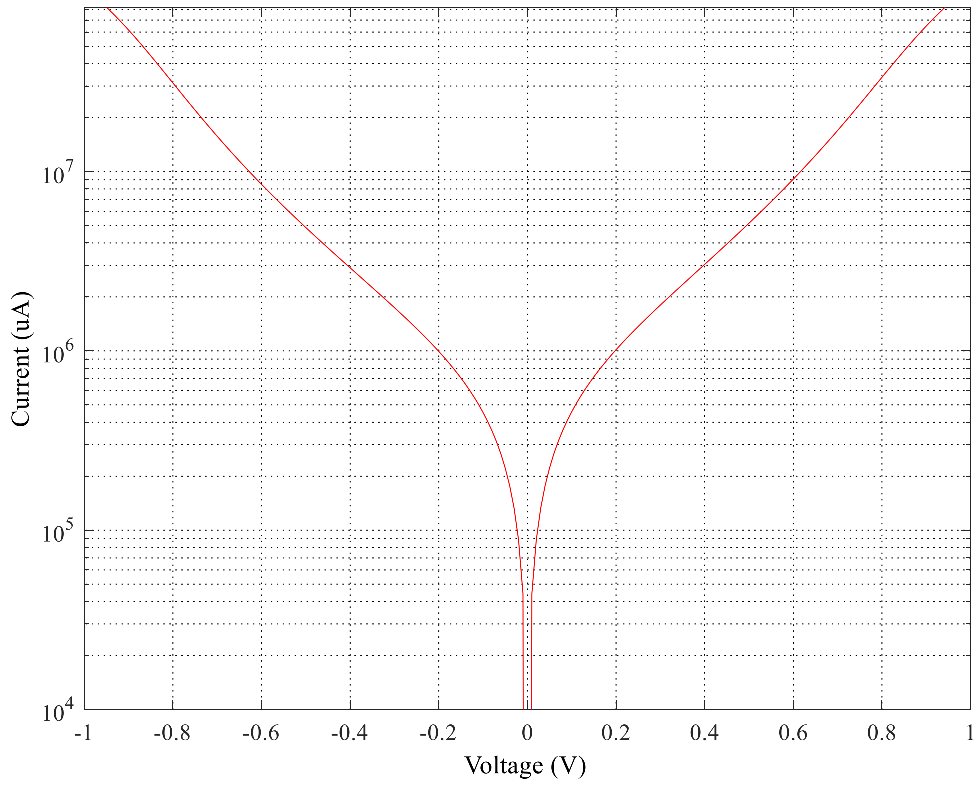

(b) Logarithmic I-V characteristic curve of 100µm^2 MIM diode with 8-Carbon atom SAM

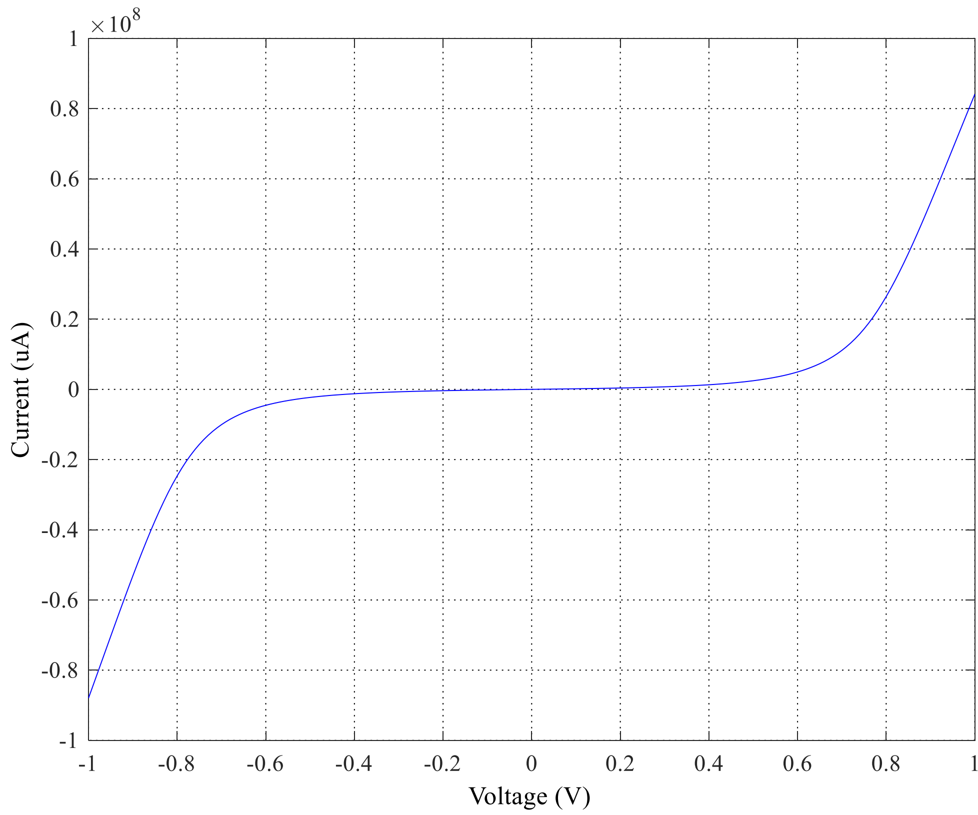

(c) I-V characteristic curve of 100µm^2 MIM diode with 10-Carbon atom SAM

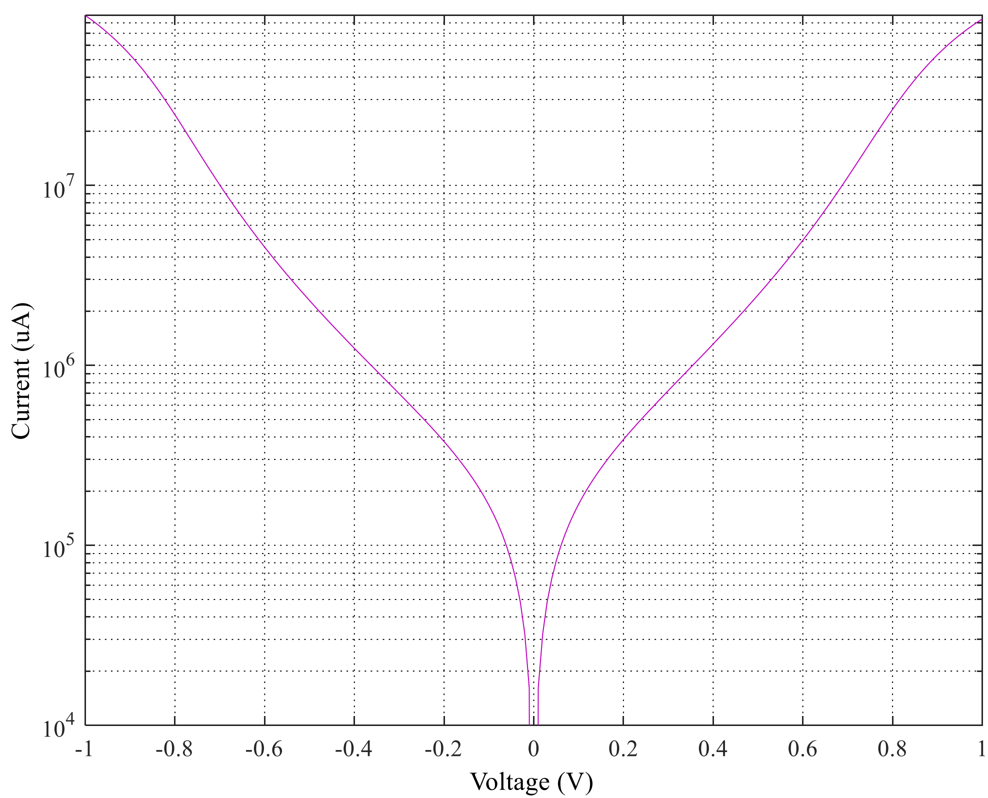

(d) Logarithmic I-V characteristic curve of 100μm^2 MIM diode with 10-Carbon atom SAM

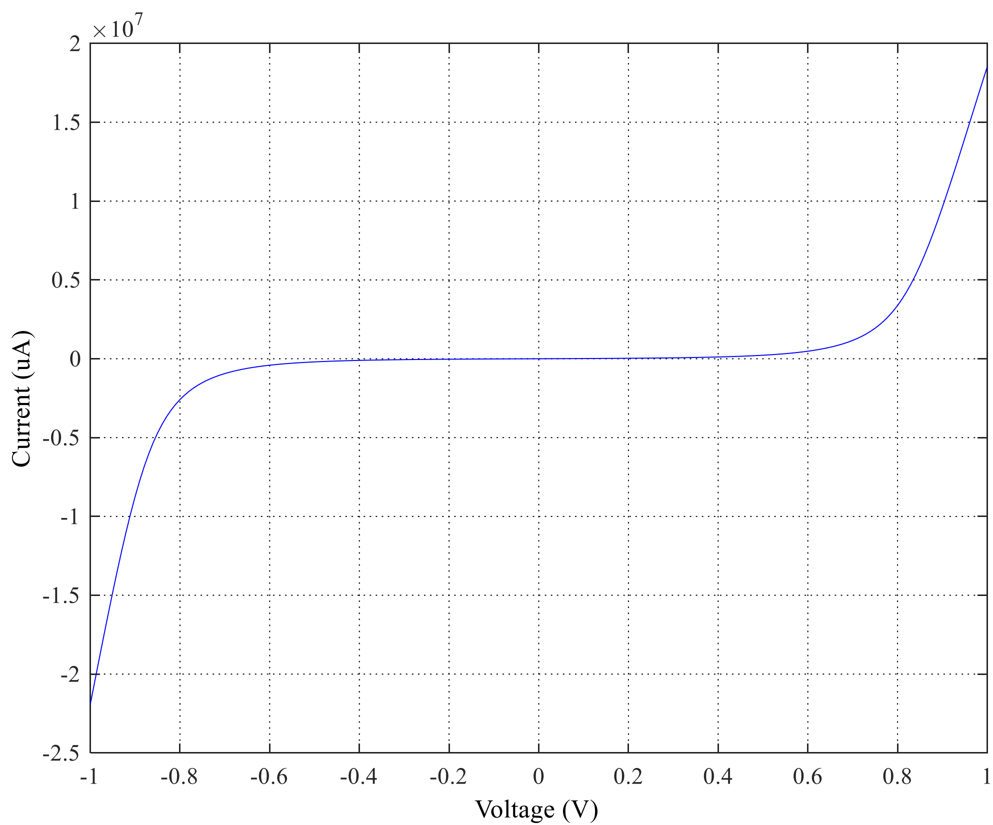

(e) I-V characteristic curve of 100μm^2 MIM diode with 12-Carbon atom SAM

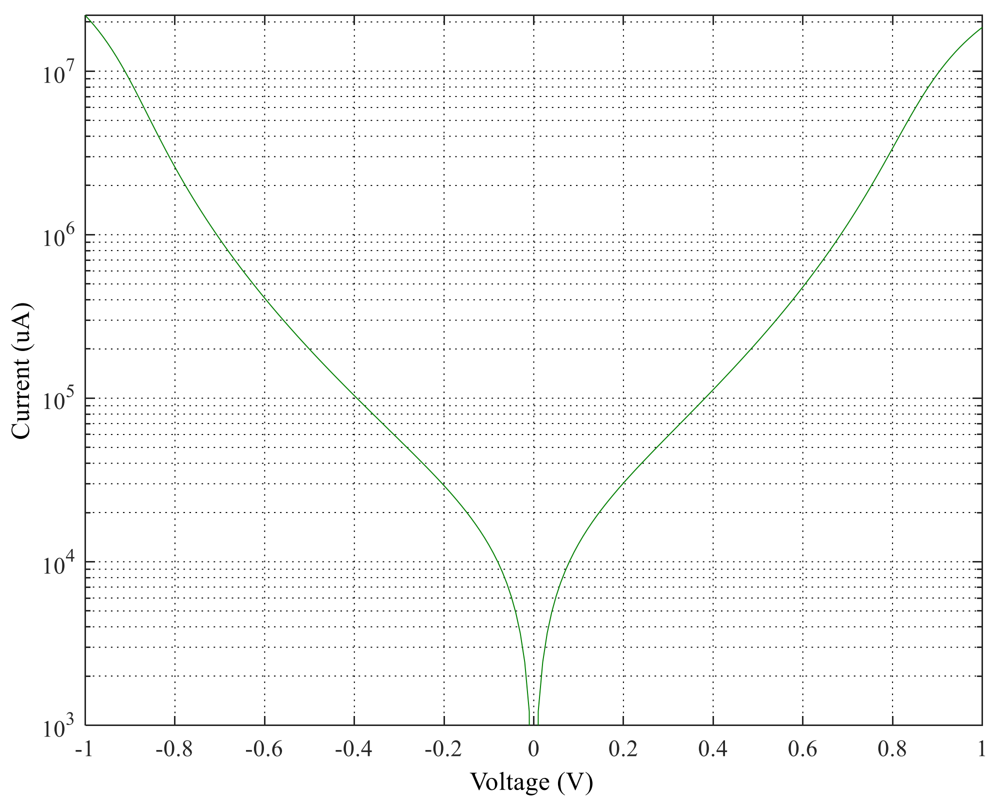

(f) Logarithmic I-V characteristic curve of 100μm^2 MIM diode with 12-Carbon atom SAM

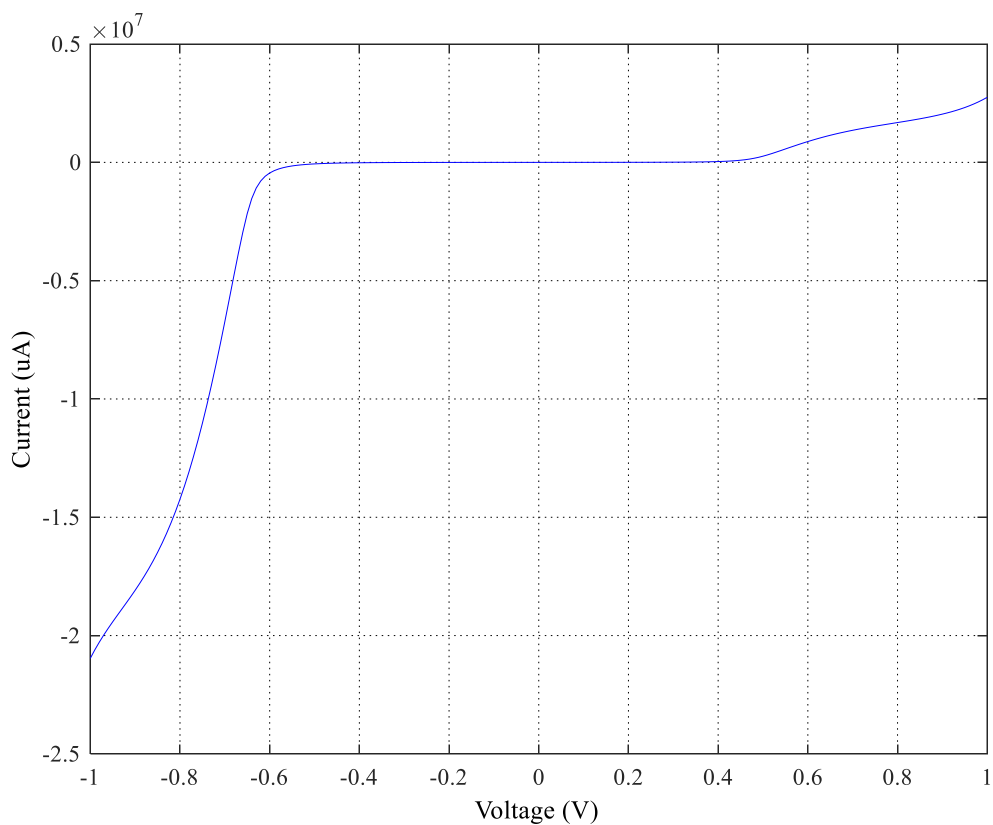

(g) I-V characteristic curve of 100μm^2 MIM diode with 18-Carbon atom SAM

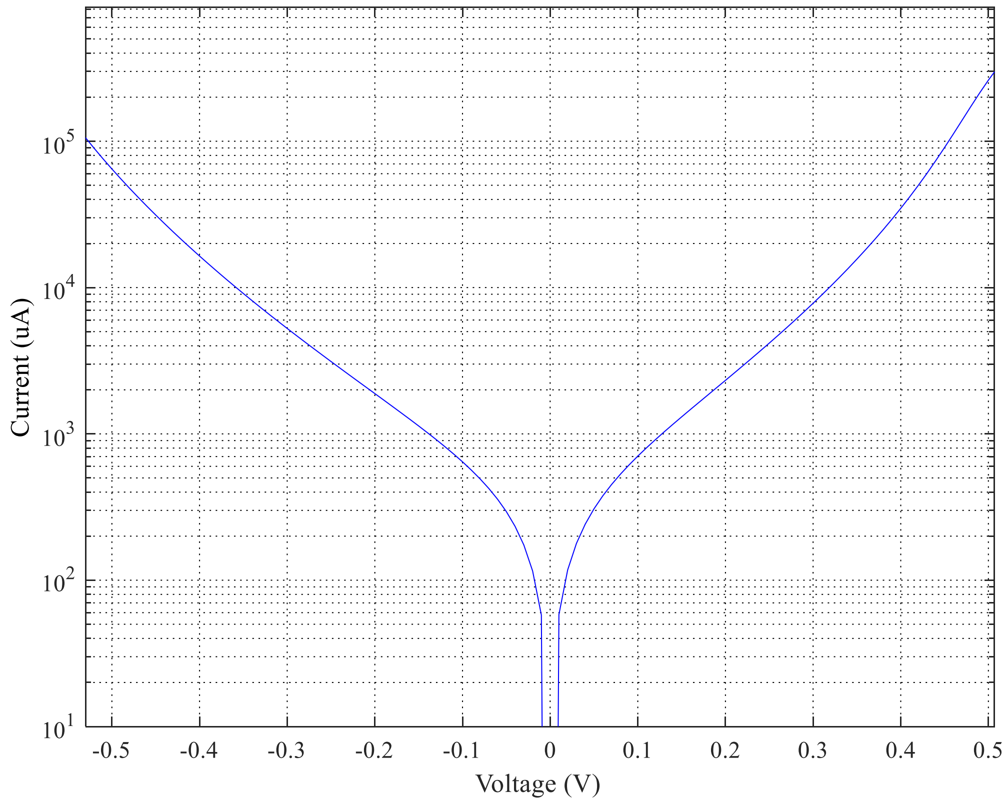

(h) Logarithmic I-V characteristic curve of 100μm^2 MIM diode with 18-Carbon atom SAM
Figure 3.8: Plots showing the I-V characteristics of fabricated MIM diodes with parameters as shown in table 3.1.

Experimental data from table 3.1 were equally used in validating the accuracy of barrier height estimation. This was done by making a plot of $log\left(\left|\frac{I}{(V+\Delta h_t)^2}\right|\right)$ versus $\left|\frac{1}{(V+\Delta h_t)}\right|$ as shown in figure 3.9. This plot was observed to be in good agreement with the work of Cowell et al [68].

It can be observed that the current in figures 3.8a, c, e, and g ranges from 2.5 A (18-carbon atoms) to as high as 100 A (8-carbon atoms); this implies that diodes fabricated from high carbon atom SAMs (18- and 12-carbon atoms) are more functional and realistic than those fabricated from low carbon atom SAMs as can be seen from the asymmetric nature of their respective I-V curves.

Asymmetry is a necessary figure of merit for the diode in a rectenna device, and it should be greater than 1 (unity), because a value of 1 indicates full symmetry (i.e. equal barrier heights at both side of the insulator) and hence no rectification [20].

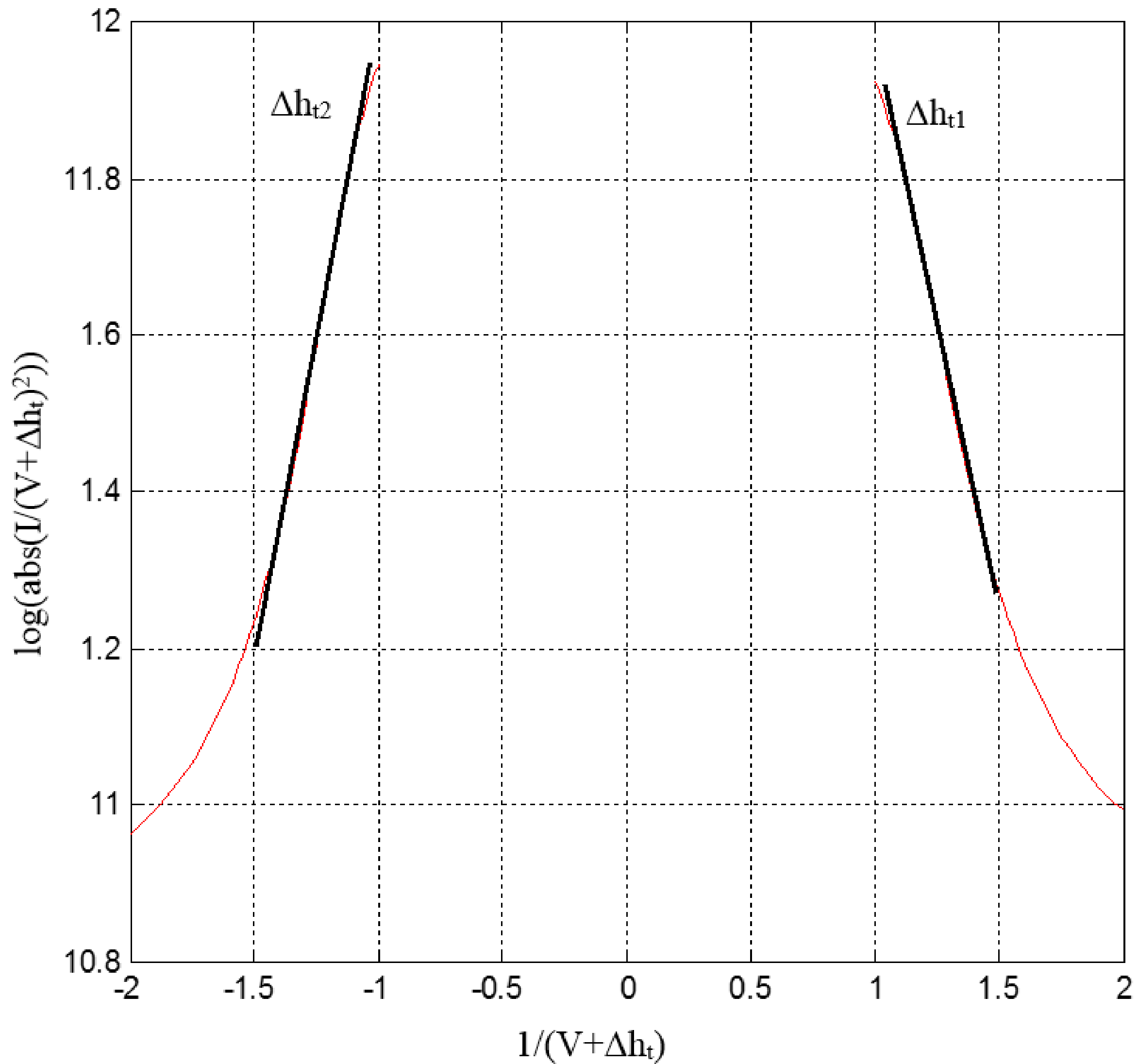

Figure 3.9: A plot of log ($|I/(V+\Delta h_t)^2|$) vs. $1/(V+\Delta h_t)$.

If this plot is properly fitted to a plot of the experimental data, the barrier heights h_{t1} and h_{t2} can be estimated to a high degree of accuracy as fit parameters, given acceptable values of the constants K_1 and K_2. A linear regression of the plot can then be used to estimate the values of the slope and intercept, *m* and *b* respectively.

The MIM diode fabricated using 18-Carbon atom SAM is the model used for this fitting. The details of the diode are: zero-bias resistance and responsivity of 5 GΩ and 8.0 V^{-1} respectively and a maximum responsivity, asymmetry and nonlinearity of 20.8V^{-1}, 117.8 and 6.8 respectively.

CHAPTER 4

DEVICE FABRICATION

4.1 Fabrication Processes

This chapter discusses the process steps that have been designed and developed which will be required in the future for the fabrication of MIM diode-based rectennas. As said previously in section 2.1.3, MIM diodes basically consists of a base metal, an insulator and a top metal.

4.1.1 Wafer processing

Four 2-inch plane borosilicate glass wafers were cleaned by heating them in a mixture of water (150 ml) and decon-90 (30 ml), at a temperature of 45 ^{0}C for 15 minutes; subsequently the wafers were heated again, at the same temperature, in deionized water alone for another 15 minutes and then dried at a temperature of 90 ^{0}C in a Medline Scientific vacuum oven.

4.1.2 Insulator preparation and deposition

Four solutions of different self-assembled monolayer (SAM) organic insulators were prepared in the glovebox. This was done by using a micropipette to measure out 20 µl volume of each insulator and adding it to 80 ml volume of hexane, which serves as the solvent. The various mixtures were sonicated for 25 minutes. The prepared organic insulators were deposited on the processed borosilicate glass wafers by immersing and soaking the wafers separately in each solution of the organic insulator and hexane, and leaving it steady without stirring for a reaction time of an hour. Afterwards, the wafers were removed from the respective solutions and immersed immediately in 4 separate beakers of hexane and then sonicated for another 15 minutes; this is to ensure that any loose SAM particles on the wafer were completely removed. After the insulator deposition, the wafers were baked for 30 minutes at a temperature of 90 ^{0}C to ensure that no residual hexane is left on the wafer surface.

The different organic insulators prepared are: BTS (butyltrichlorosilane, 4-carbon atoms), OCTS (octyltrichlorosilane, 8-carbon atoms), DTS (decyltrichlorosilane, 10-carbon atoms) and

OTS (octadecyltrichlorosilane, 18-carbon atoms). The first three have the same chemical constituents and structure as the Octadecyltrichlorosilane already shown in figure 2.1, with the only difference being in their respective numbers of carbon atoms.

4.1.3 Determination of water contact angles (*WCA*)

The contact angles a drop of water (5 µl) made on the respective insulator-coated wafer surfaces were measured in order to determining the hydrophilicity and hydrophobicity of the surfaces. This was done with a view to determine how compact and tight the atoms in a molecule of the insulator are, thus giving an indication of the uniformity of the surface. A smaller contact angle indicates a more hydrophilic surface while a larger contact angle indicates a more hydrophobic surface (with more compact and tight molecular atoms).

The images of a 5 µl drop of water on two wafer surfaces, as analysed using the image processing toolbox of Matlab®, are shown in figures 4.1a and 4.1b. Figure 4.1a shows the image of the drop and the contact angle it made just before insulator deposition. This is a good indication of the hydrophilic nature of glass which like aluminium is easily wetted (i.e. oxidizes when exposed to air). Figure 4.1b shows the same drop, (5 µl), and the contact angle it made on the wafer surface coated with BTS.

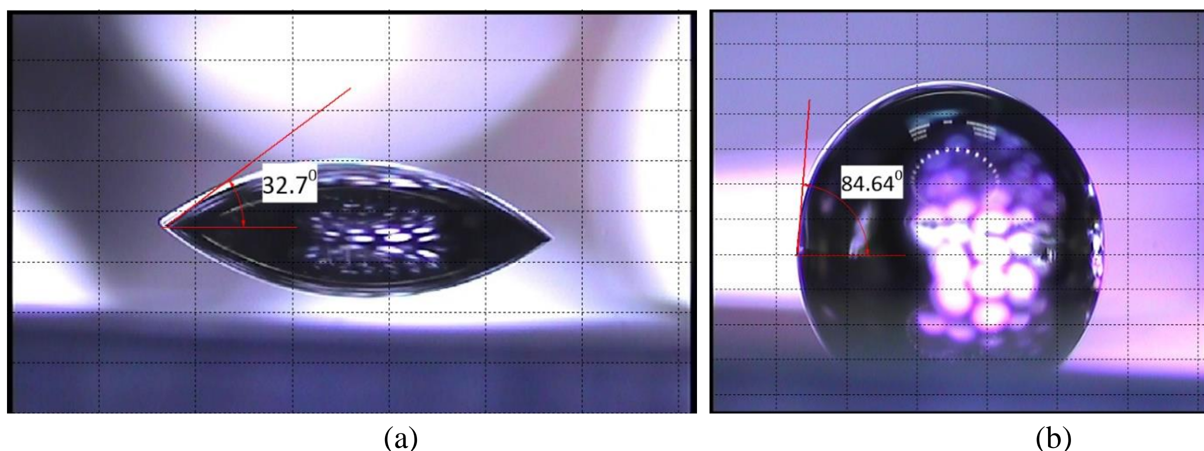

(a) (b)

Figure 4.1: 5µl drop of water on (a): wafer without SAM and (b): wafer coated with BTS.

The contact angles made by the water droplet on the respective wafer surfaces are shown in Table 4.1. It can easily be observed that the drop made larger contact angles on the wafer surfaces coated with the organic insulators than it made on the plane surface before being coated with the insulators. In addition to that, the contact angles were increasing as the number of carbon atoms in a chain of the molecule of the organic insulator increased. This implies that the greater the number of carbon atoms, the more compact and tight the molecules of the organic insulator; hence the monolayer formed will be more uniform with minimal pinholes and thus more hydrophobic.

Table 4.1: Water droplet contact angles on the respective wafer surfaces.

Surface preparation	Contact angle of water on surface
Plane borosilicate glass	32.7^0
Butyltrichlorosilane (BTS)	84.6^0
Octyltrichlorosilane (OCTS)	87.1^0
Decyltrichlorosilane (DTS)	90.0^0
Octadecyltrichlorosilane (OTS)	90.0^0

4.1.4 Atomic force microscope (*AFM*) *imaging*

A plane borosilicate glass and the insulator-coated wafers were scanned with the atomic force microscope, and scanned images were taken. The scan, which was conducted in two modes (tapping and Tunnelling AFM (TUNA) contact modes), was done to help in the analysis of the respective wafer surfaces and to ascertain the degree of insulation provided by the dielectric (organic insulator) films on the wafer surfaces.

Surface topography images of the plane borosilicate glass and the 4 insulator-coated wafers are shown in figures 4.2a - 4.2e. These images were taken during tapping-mode scanning. Significant visual differences in topography can be observed from the images, these are as a result of the differences in the number of carbon atoms in a chain of a molecule of the organic insulators. It is still worth noting that of the 4 organic insulators, the surfaces of the 8- and 10-carbon atom insulators (OCTS and DTS) have a close similarity when compared with those of

4- and 18- carbon atoms (BTS and OTS), this is due to the closeness in their numbers of carbon atoms. The greater the number of carbon atoms, the more compact and tight are the molecular bonds of the organic insulator, hence molecular compactness and tightness of the bonds between the molecules of the dielectric are requirements for surface uniformity and larger contact angle, which is a measure of surface hydrophobicity.

The surface topography image of the wafer coated with BTS (figure 4.2a) can be said to bear a resemblance to the surface topography image of the plane borosilicate glass (figure 4.2e). The reason for this similarity is that the length of the non-polar alkyl tail which forms the monolayer-thick canopy on the wafer surface is very small in BTS unlike the case of other insulators (figures 4.2b, c, and d).

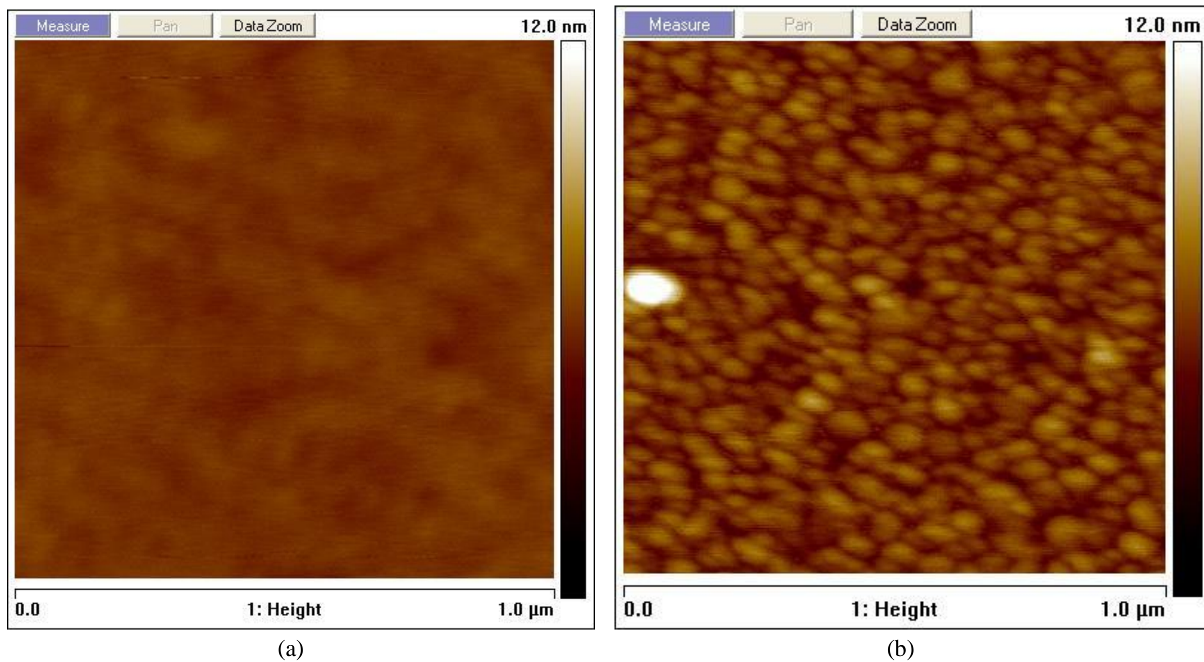

(a) (b)

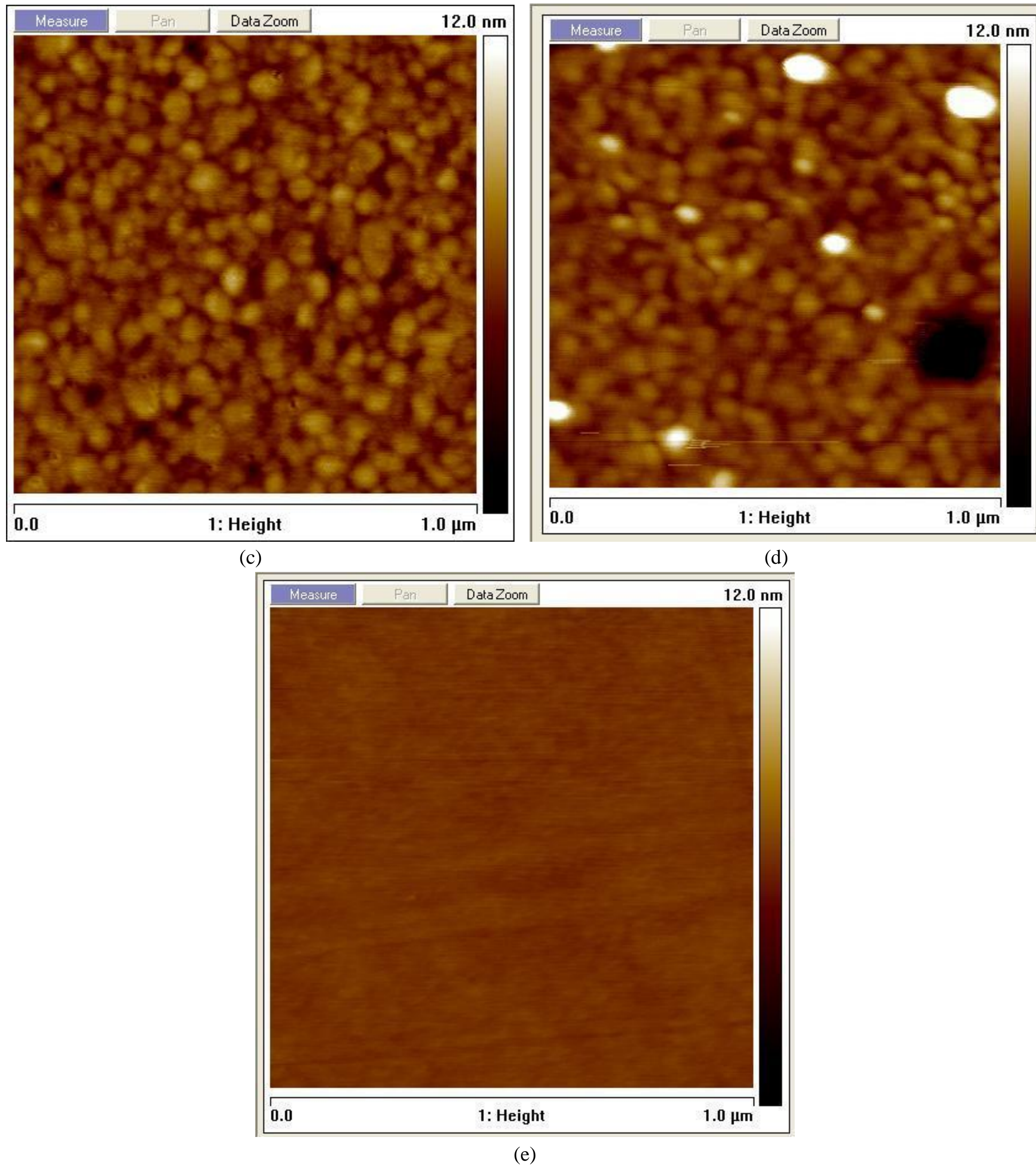

Figure 4.2: Surface topography images of (a): BTS coated wafer (area of $1\mu m^2$); (b): OCTS coated wafer (area of $1\mu m^2$); (c): DTS coated wafer (area of $1\mu m^2$); (d): OTS coated wafer (area of $1\mu m^2$) and (e): A plane borosilicate glass (area of $1\mu m^2$)

A schematic representation of the configuration for TUNA contact scanning, which is basically done for determining the insulating capacity of the dielectric layer, is shown in figure 4.3a, while the scan image obtained is shown in figure 4.3b. During this scanning mode, a DC bias voltage V_{bias} = 2 V was applied to the substrate, then the current flowing between the substrate and the AFM tip was measured, using the ammeter A, as shown in figure 4.3a.

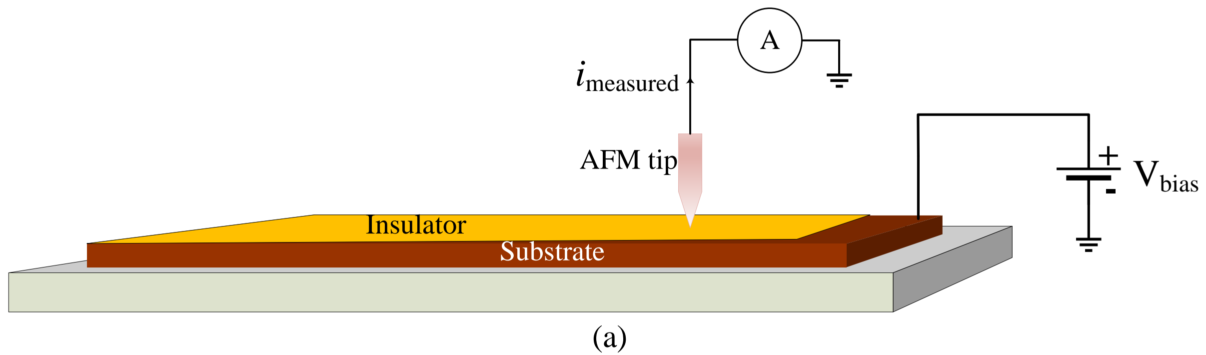

(a)

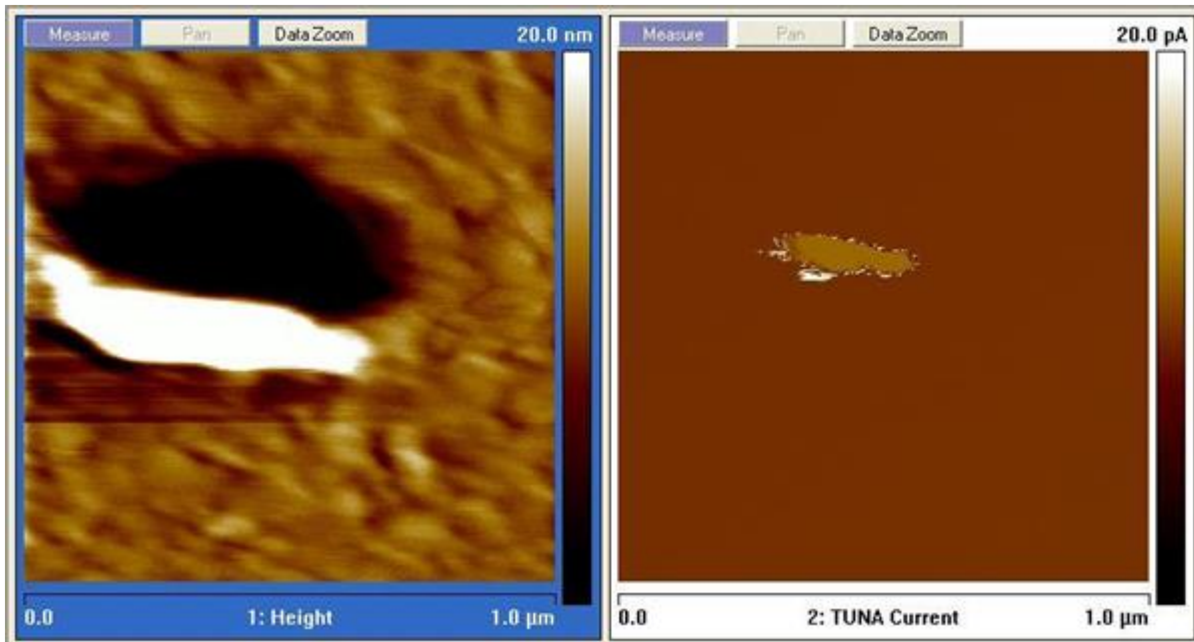

(b)

Figure 4.3: (a) Schematic of TUNA scan configuration and (b) TUNA surface topography for OTS as well as the TUNA current through the OTS dielectric layer.

Surface roughness plays a critical role in the appearance and adhesion of coatings. The root mean square (RMS) roughness values for the plane borosilicate glass and insulator-coated wafers are shown in table 4.2. It can be observed from the table that the values of the RMS roughness are different; with the plane glass having the least value of 0.157 nm. Comparing the RMS roughness values of the 4 insulator-coated wafers reveals that the wafers on which the water droplet made the least and largest contact angles have the lowest and highest roughness values of 0.23 nm and 1.55 nm respectively thus confirming the observations of Guo-Hua et al and Song et al [71, 72] that surface roughness contributes to larger contact angle.

Table 4.2: RMS roughness of plane borosilicate glass and insulator-coated wafers.

Surface (1μm^2)	RMS roughness (nm)
Plane borosilicate glass	0.157
Butyltrichlorosilane (BTS)	0.23
Octyltrichlorosilane (OCTS)	0.888
Decyltrichlorosilane (DTS)	0.894
Octadecyltrichlorosilane (OTS)	1.55

The investigated SAMs can be exploited in a practical rectenna by:

1. Depositing the SAMs on the base metal (Titanium in this research work) which will act as the anode electrode.

2. Heating the base metal with the deposited SAM for 30mins at a mild temperature below the flash point temperature of the respective SAMs; (45 ^{0}C for BTS, 96 ^{0}C for OCTS, 110 ^{0}C for DTS and 189 ^{0}C for OTS) in accordance with Alfa Aesar®, the manufacturer's, safety data sheets. The essence of this heating process is to ensure the proper polymerization of the SAM molecules.

3. Depositing the top metal (Platinum in this research work) which will then acts as the cathode electrode to complete the fabrication process.

4.2 Process steps for MIM junction fabrication

The procedures for device fabrication are in two phases as detailed below.

PHASE 1

1. Wafer processing: Four 2-inch borosilicate glass wafers were cleaned by heating them in a mixture of water (150 ml) and decon-90 (30 ml), at a temperature of 45 ^{0}C for 15 minutes; subsequently the wafers were heated again, at the same temperature, in deionized water alone for another 15 minutes and then dried at a temperature of 90 ^{0}C in the oven (Medline Scientific OV-11).

2. Spin-Coating with Photoresists: The wafers were then spin-coated with polydimethylglutarimide (PMGI SF-9) lift-off resist and megaposit SPR-350 positive resist. Positive resists dissolve the UV-illuminated areas of the wafer (areas exposed to UV-rays), during wafer development unlike negative resists which dissolve the unexposed areas of the wafer during development. PMGI, an alkaline soluble polymer derived from polymethylmethacrylate (PMMA), is often spin-coated beneath photoresists to serve as a lift-off resist in multilayer lithography where an undercut is needed. The spin-coating conditions and timing are shown in table 4.3.
3. UV exposure: This is the process of transferring or imprinting patterns from a photomask onto a resist-coated wafer by exposing the mask and wafer to high temperature UV rays using the electronic vision group machine (EVG-620). A photomask is an opaque plate with defined transparencies tracing a pattern. Two masks were used because the fabrication process is bi-layer, in which case the crossover of the two layers will be the position of the diode. The first photomask was exposed with the wafers at an energy level of 65 mJ/cm^2, with vacuum-hard (V+H) as the contact mode.
4. Wafer development: After exposition in the EVG, the wafers were developed using MF 319 Microposit developer (constituents of the developer are: Water = 98% and tetramethylammonium hydroxide = 2%). This was done by moving the wafers gently in the developer solution for 60 seconds; afterwards the wafers were rinsed two consecutive times in a beaker containing deionized water, and subsequently dried with nitrogen gas.
5. Metallization: This entails the deposition of metals (titanium 25nm thick and gold 100nm thick) on the patterned wafer samples, and the process is normally done using the Moorfield minilab 080 e-beam evaporation system. The gold is normally deposited on the titanium to prevent the titanium from being oxidized.

6. Lift-off: This is the process of immersing the metallized patterned wafers in a beaker containing microposit remover-1165, and heating it gently at a mild temperature of 65 ^{0}C. The PMGI is dissolved by the microposit remover-1165 thereby lifting-off all the metal and resist on the unilluminated portions of the wafers. After lift-off, the deposited metal remains only on the initially exposed portions of the wafers from where the positive resist was dissolved by the MF 319 developer. After the 1165 has stripped the photoresist off, the wafers were then immersed in acetone and sonicated for 2 min, before rinsing in isopropanol (IPA) and DI water.

PHASE 2

1. Spin-Coating: The wafer samples were spin-coated again using the same resists as in the first phase.
2. UV exposure: This process is similar to the UV exposition done in phase 1, the only difference being that the second mask is exposed with the wafers instead of the first mask, and this second mask must be set in order to cross-arm the metallized pattern of the first mask on the wafer samples.
3. Wafer development: This is exactly the same process as in the first phase.
4. Etching (gold etching): Gold etching was done by pouring the etch solution (potassium iodide, iodine and deionized water in the ratio of 4:1:8 respectively) in a beaker, and immersing the wafers in the solution for 20 seconds so that only the gold on the exposed cross-arm of the two-mask patterns will be etched off, thereby exposing the titanium on the cross-arm.
5. Insulator preparation and deposition: The self-assembled monolayer (SAM) organic insulators were prepared in the glovebox, using a micropipette to measure out 20 µl volume of each insulator and adding it to 80 ml volume of hexane, which serves as the solvent. The various mixtures were then sonicated for 25 minutes and deposited on the

processed borosilicate glass wafers by immersing and soaking the wafers separately in each solution of the organic insulator and hexane. The setup is left steady without stirring for a reaction time of an hour which afterwards, the wafers were removed from the respective solutions and immersed immediately in 4 separate beakers of hexane and then sonicated for another 15 minutes; this is to ensure that any loose SAM particles on the wafer were completely removed. After the insulator deposition, the wafers were baked for 30 minutes at a temperature of 90^{0}C to ensure that no residual hexane is left on the wafer surface.

6. Metallisation: This entails the deposition of the top metal layer Platinum, 40nm in thickness, to complete the MIM diode fabrication.

Table 4.3: Spin-coating Conditions and Timing

Process	Condition	Time
Wafer dehydration bake	200°C	3 mins.
Spin PMGI SF9	500 rpm	10 secs.
Spin PMGI SF9	6000 rpm	50 secs.
Bake	200°C	5 mins.
Spin Microposit SPR 350	700 rpm	10 secs.
Spin Microposit SPR 350	3700 rpm	40 secs.
Bake	110°C	3 mins.
Expose to UV in EVG		
Develop (MF 319)		60 secs.
Metallise		

4.2.1 Diagrammatic representation of the device fabrication processes

The proposed fabrication process for a complete MIM junction is shown in figure 4.4.

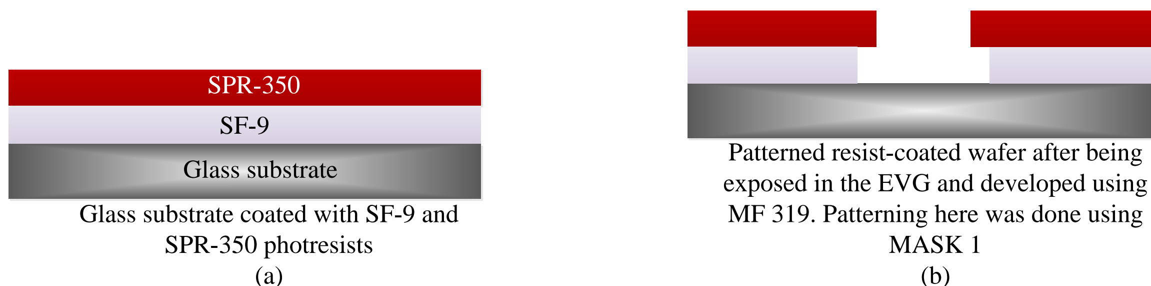

Glass substrate coated with SF-9 and SPR-350 photresists
(a)

Patterned resist-coated wafer after being exposed in the EVG and developed using MF 319. Patterning here was done using MASK 1
(b)

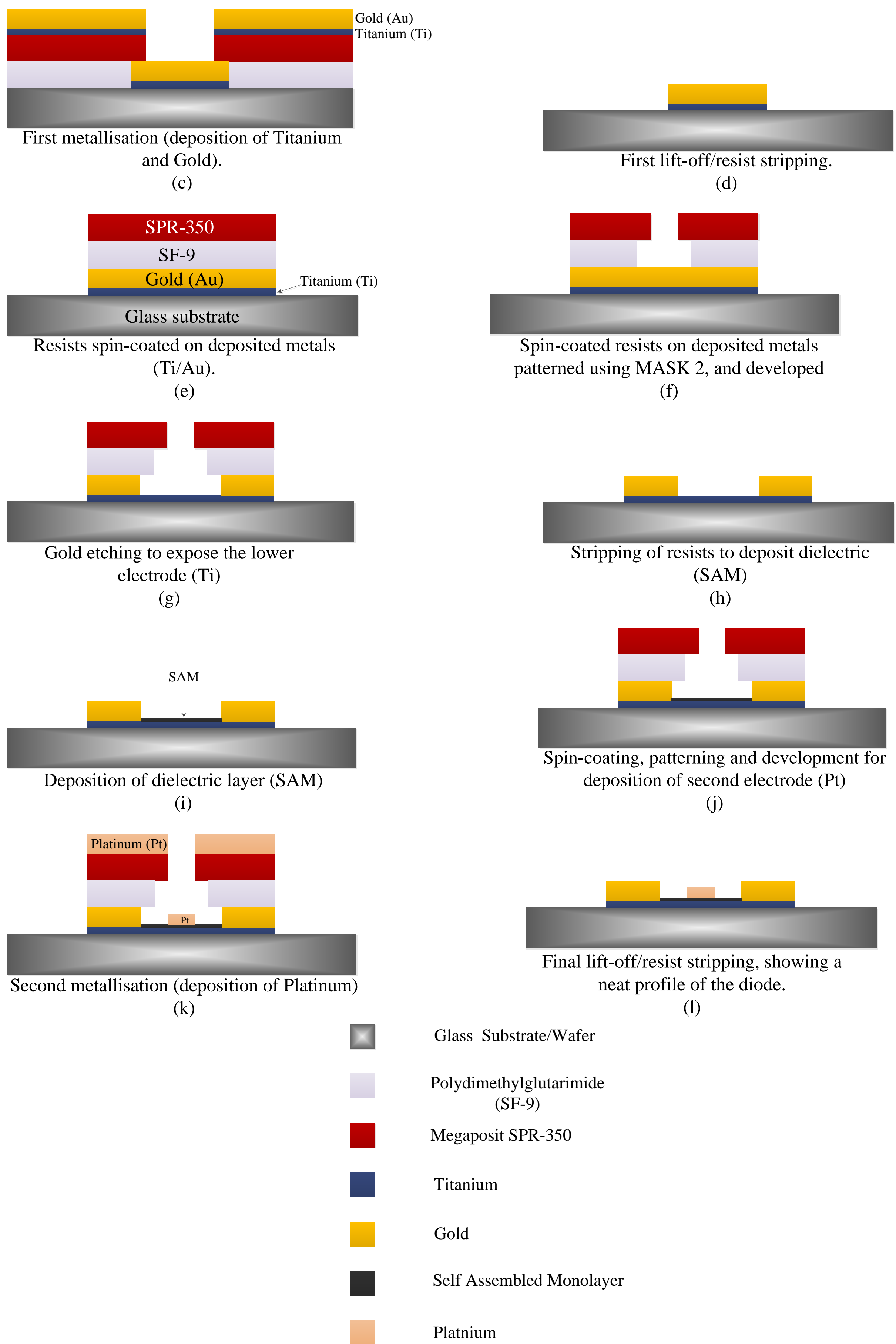

Figure 4.4: A pictorial representation of the bi-layer fabrication process steps.

Although all the experimental process steps discussed above were not carried out, (the metallization stage of phase 2, deposition of Platinum, was not done), the main experimental achievement is the precision and accuracy in keeping to the spin-coating conditions as well as during wafer development.

CHAPTER 5

INSTRUMENTATION FOR DIODE CHARACTERISATION

Electrical characterisation of devices is typically carried out in order to determine device parameters such as the carrier doping density, type and mobility of carriers, parasitic resistances as well as resistivity, nonlinearity, conductivity, interface quality, dielectric trap density, barrier height etc. This is normally done in order to ascertain the quality and reliability of the device.

In this research work, diode characterisation was done to determine three main parameters which are: the current-voltage (I-V) characteristic curve, differential conductance, and nonlinearity.

The key instruments used to build the electrical characterization setup are:

i. AMATEK 7230 DSP lock-in amplifier

ii. Voltage combiner/current-voltage converter

iii. 4 extra heavy duty 9V dry batteries

5.1 Low frequency (LF) Characterisation

In order to perform LF characterisation, the diode is connected to two electrodes, signal and ground ports, of the voltage combiner/I-V converter which is powered. This voltage combiner/I-V converter is connected to the lock-in amplifier which is linked to a local area network (LAN). It is the lock-in amplifier that provides the AC signal of given amplitude and frequency across the diode. Using a MATLAB® code, the readings of the rectified current are taken over a voltage range which is specified in the program. The essence of low frequency characterisation is to determine three major parameters of the diode which are the I-V (current-voltage) characteristic, differential conductance, and nonlinearity. From these, other figures of merits such as responsivity, differential resistance and asymmetry can easily be determined.

A sinusoidal signal is applied across the diode, and the amplitude of the applied signal is measured at the fundamental and second harmonic frequency. Mathematically the instantaneous current, I, is expressed by the Taylor series:

$$I = I_S\left[a\frac{V}{V_{th}} + b\left(\frac{V}{V_{th}}\right)^2 + \ldots\ldots\right] \qquad (5.1a)$$

where I_S is the peak current, $a \propto \frac{dI}{dV}$, $V = A\cos\omega_0 t$ is the applied voltage, V_{th} is the thermal voltage, and $b \propto \frac{d^2I}{dV^2}$. Further evaluation of (5.1a) gives:

$$\frac{I}{I_S} = \frac{bA^2}{2V_{th}^{\ 2}} + \frac{aA}{V_{th}}\cos\omega_0 t + \frac{bA^2}{2V_{th}^{\ 2}}\cos(2\omega_0 t) \qquad (5.1b)$$

It is worth noting that the first term of (5.1b) is a dc component of the current, while the second and third terms are the fundamental f_0 and second harmonic $2f_0$ frequency components respectively.

A schematic circuit representation of the LF characterisation principle and a pictorial representation of the actual setup used for the characterisation is shown in figures 5.1 and 5.2 respectively.

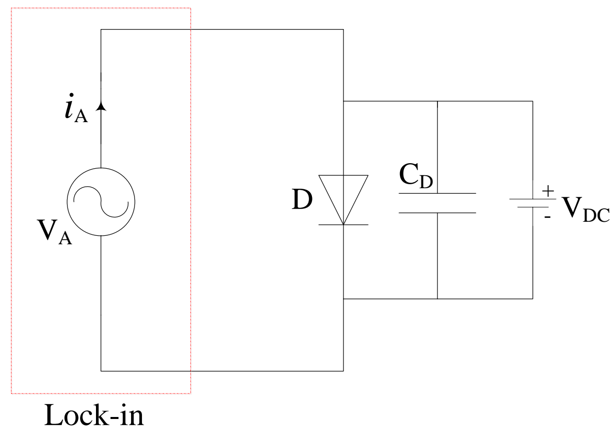

Figure 5.1: Schematic circuit representation of low frequency characterisation of the diode, D. V_A represents the AC source from the lock-in, C_D represents the diode junction capacitance, while V_{DC} represents the applied DC bias.

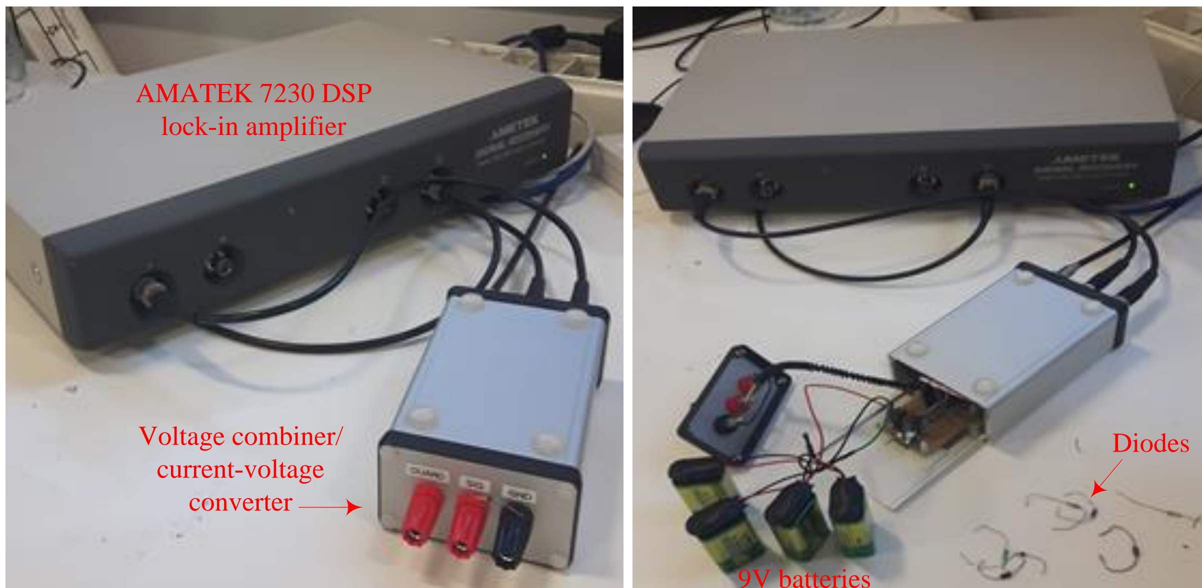

Figure 5.2: Pictorial representation of the actual setup used for the characterisation

The values of the sinusoidal signal amplitude, frequency, fundamental and second harmonic phases are all set as well as varied from the lock-in amplifier main control panel.

5.2 Validation of low frequency measurement setup

The low frequency measurement setup was validated using ordinary p-n junction (1N4007) and Zener diodes. An AC signal with amplitude 1 mV and frequency 1 KHz was provided across the diodes. The AC amplitude value of 1 mV was chosen because it is less than the room temperature thermal voltage of the diode which is 25 mV, secondly MIM diode for energy harvesting needs to operate at zero bias voltage, and 1 mV is such a small enough value. The

amplitude of the current at f_0 and $2f_0$ was then measured over a voltage range, and a program coded in Matlab® was used in plotting the I-V characteristics, differential conductance as well as the nonlinearity curves of the diodes. Shown in figures 5.3 and 5.4 are typical plots used in validating the low frequency measurement setup for the two diodes.

The presence of a capacitance across the diode junction results to an AC leakage current through the diode capacitor. The two I-V curves (coloured blue and red) shown in the figures are estimated from the 1st and 2nd derivatives of the diode current respectively. The second derivative (red curve) does not suffer from such leakage component.

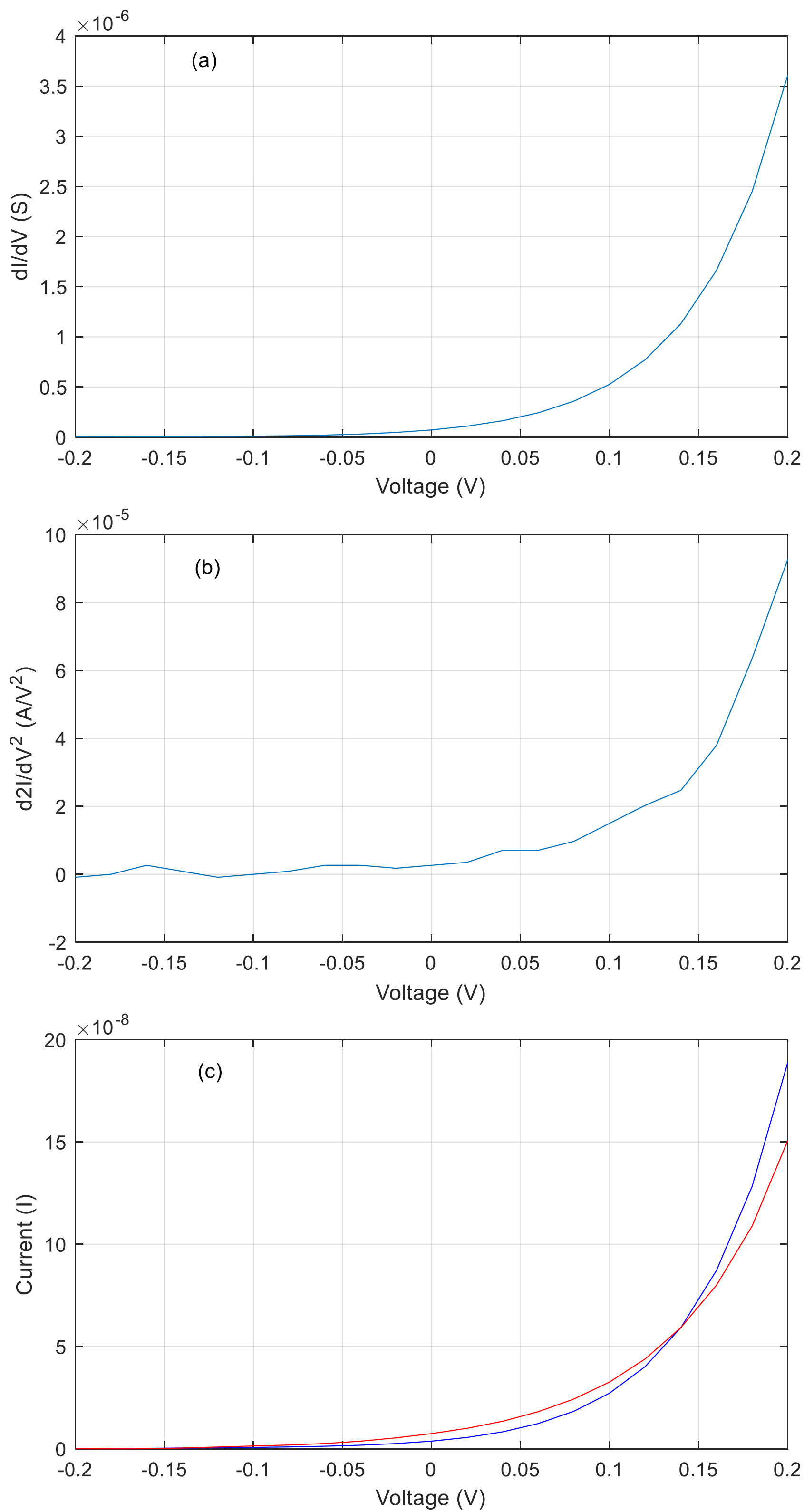

Figure 5.3: Plots showing (a) differential conductance, (b) nonlinearity and (c) I-V characteristic curves of a zener diode with the sensitivities for f_o & $2f_o$ set at 2mV and 200µV respectively and a time constant of 1sec.

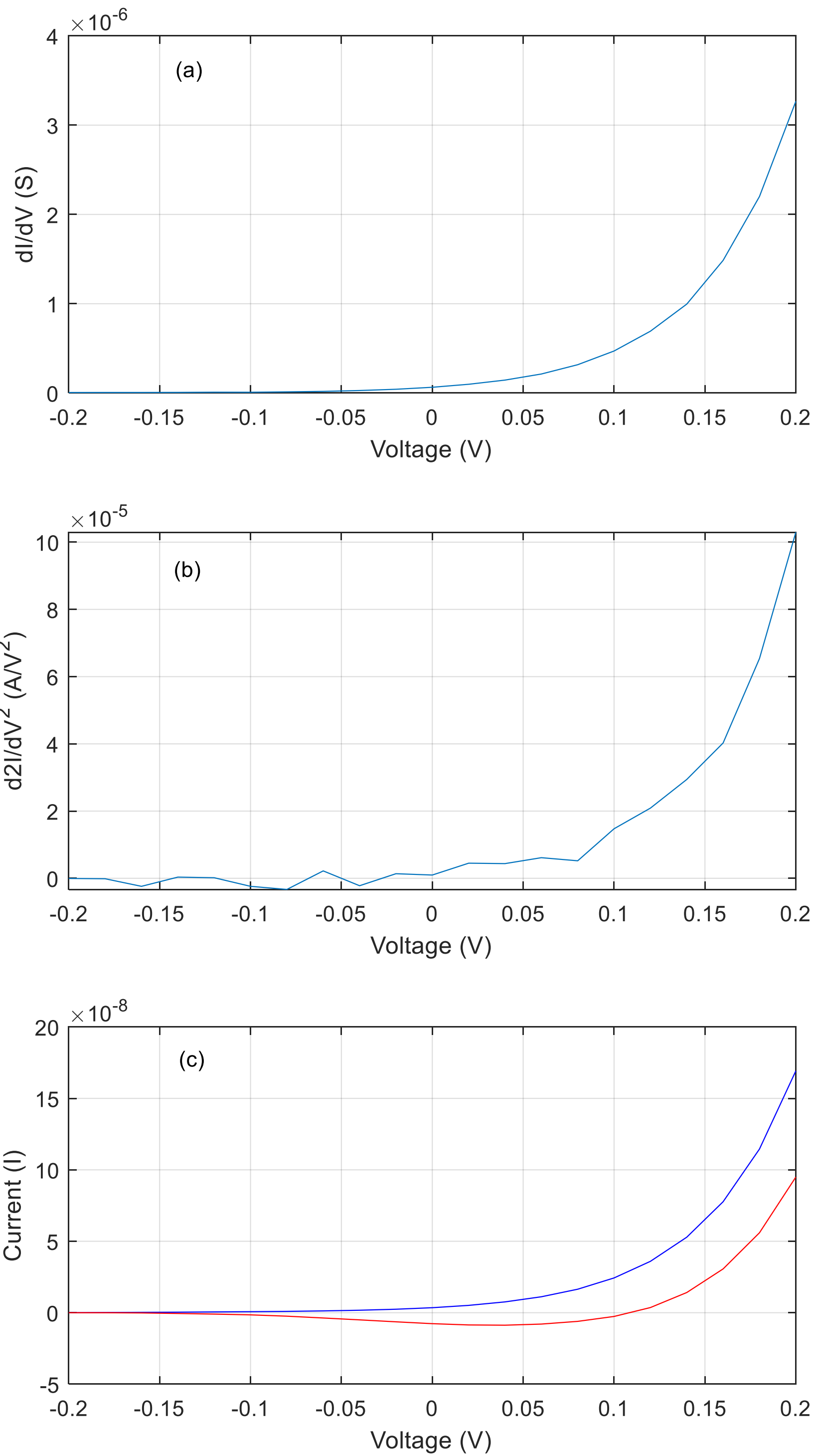

Figure 5.4: Plots showing (a) differential conductance, (b) nonlinearity and (c) I-V characteristic curves of an ordinary 1N4007 junction diode with both sensitivities for f_o & $2f_o$ set at 2mV and a time constant of 1sec.

CHAPTER 6

CONCLUSIONS AND FUTURE WORK

6.1 Conclusion

An overview of thermal energy conversion using rectenna technology has been presented and the key factors for realising an optimally efficient device well highlighted. A temperature profile measurement of an automobile engine and exhaust was made with a view to determine the operable temperature ranges of an automobile. The values obtained from this measurement are essential for calculating the dimension of the antenna in a rectenna device, since the outer antenna dimension depends on the target frequency range which is a function of the source temperature.

The contact angles made by a 5 μl droplet of water on wafer surfaces coated with thin films of the self-assembled monolayer (dielectric) were measured in order to determine the hydrophilicity and/or hydrophobicity of the dielectric films. This gives an idea of how compact and tight the atoms in a molecule of the dielectric film are, thus giving an indication of how uniform a surface coated with such dielectric film will be. A set up for the low frequency characterisation of the diode was made and validated using ordinary diodes.

6.2 Future work

The challenge to develop a practical and functional rectenna device has given rise to a reasonable number of research works in the field, of which some are listed in table 2.1. A vast majority of these works have poor impedance matching as a major limitation. Therefore carefully following the process steps of section 4.2 to fabricate an MIM tunnelling diode, and developing a very good broadband impedance matching structure for matching the antenna and diode impedances will make feasible a practical and functional rectenna device.

6.2.1 Terahertz Characterisation

Since MIM diodes are fundamentally high frequency (terahertz range) diodes, with operational frequency within the target frequency range of this research work, there is need for terahertz characterisation of the fabricated diode, which is proposed in this section. This is normally done using a terahertz emitter as a source. A mechanical chopper is placed between the source and the rectenna device, which is placed at some distance from the source. The rectenna is then connected to a lock-in amplifier as shown in figure 6.1. The chopper makes it possible for the rectenna device to be intermittently exposed to terahertz signals from the source, while the output signals from the device are read out via the lock-in amplifier. This intermittent exposure from the chopper creates oscillatory on-and-off signals which can be read out in phase to maximise signal-to-noise (SNR) ratio.

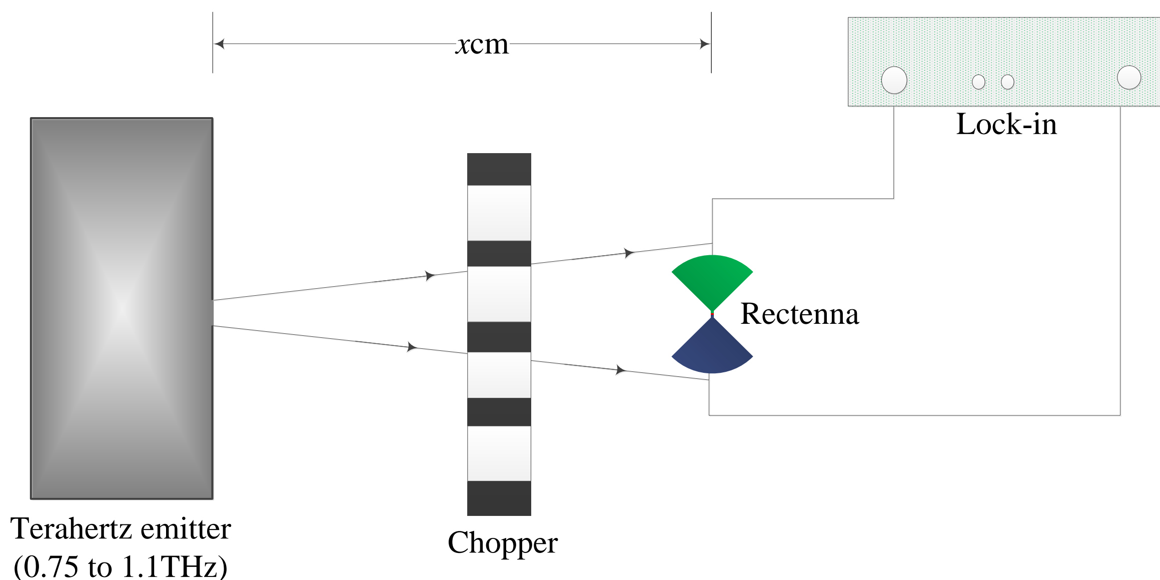

Figure 6.1: Terahertz characterisation setup for the rectenna device.

REFERENCES

[1] http://www.iop.org/resources/energy/index.html, Accessed online: 05 June, 2018.

[2] K. Gaurav and S. K. Pandey, “Efficiency calculation of a thermoelectric generator for investigating the applicability of various thermoelectric materials,” J. Renewable Sustainable Energy, vol. 9, No.14701, Feb, 2017, https://doi.org/10.1063/1.4976125

[3] Y. Pan, C. V. Powell, A. M. Song and C. Balocco, “Micro rectennas: Brownian ratchets for thermal-energy harvesting,” Applied Physics Letters 105, 253901 2014. [Online]. Available: http://dx.doi.org/10.1063/1.4905089

[4] Y. A. Çengel, “Fundamentals of Thermal Radiation,” in *Heat Transfer: A Practical Approach*, California, USA: WBC McGraw-Hill, 1998, ch. 11, pp. 580–623.

[5] L. E. Dodd, “Fabrication Optimisation of Metal-Oxide-Metal Diodes”, Ph.D. dissertation, School of Engineering and Computing Sciences, Durham Univ., Durham, UK, 2014. Online: http://etheses.dur.ac.uk/9474/

[6] W. Yang, S. Chou, C. Shu, H. Xue and Z. Li, “Research on micro-thermophotovoltaic power generators with different emitting materials,” *Journal of Micromechanics and Microengineering*, vol. 15, no. 9, pp. S239–S242, September 2005. [Online]. Available: http://dx.doi.org/10.1088/0960-1317/15/9/S11

[7] W. M. Yang, S. K. Chou, C. Shu, Z. W. Li and H. Xue, “Research on micro-thermophotovoltaic power generators” *Solar Energy Materials & Solar Cells* vol. 80, no. 1 pp. 95–104, October 2003. [Online]. Available https://www.sciencedirect.com/science/article/pii/S0927024803001351

[8] Y. Ismail and A. Alaskalany, ‘Thermoelectric Devices: Cooling and Power Generation’ https://arxiv.org/abs/1403.3836?context=cond-mat. Accessed online: 05 June, 2018.

[9] F. Stabler, “Automotive Thermoelectric Generators: Design and Manufacturing,” in Symposium N: *Material and devices for Thermal-to-Electric Energy conversion, Proc. MRS Spring Meeting*. San Francisco, California, USA, 13 April, 2009, p.9.

[10] B. Berland, Photovoltaic Technologies Beyond the Horizon: Optical Rectenna Solar Cell, subcontractor report; National Renewable Energy Laboratory, 2002. https://www.nrel.gov/docs/fy03osti/33263.pdf

[11] A. Haque, A. W. Reza and N. Kumar, “A Novel Design of Circular Edge Bow-Tie Nano Antenna for Energy Harvesting,” *Journal of RF-Engineering and Telecommunication* 2015. [Online]. Available: https://doi.org/10.1515/freq-2015-0037

[12] A. De Vos, "Thermodynamics of radiation energy-conversion in one and in three physical dimensions," *J. Phys. Chem. Solids*, vol. 49, pp. 725–730, 1988.

[13] M. Sarehraz, K. Buckle, T. Weller, E. Stefanakos, S. Bhansali, Y. Goswami and S. Kishnan, (Jan. 2005). Rectenna developments for solar energy collection. Presented at 31st IEEE Photovoltaic Specialists Conference, 3-7 Jan. 2005, Lake Buena Vista, FL, USA. [Online]. Available: https://ieeexplore.ieee.org/document/1488073/

[14] S. Joshi, S. Grover and G. Moddel, "Efficiency Limits for Solar Spectrum Rectification", in *Rectenna Solar Cells*, Moddel G., Grover S. (eds). New York, NY, USA: Springer, 2013, ch. 3, pp. 47-67.

[15] S. Grover and G. Moddel, "Applicability of Metal/Insulator/Metal (MIM) Diodes to Solar Rectennas", *IEEE Journal of Photovoltaics*, vol. 1, no. 1, Jul. 2011. http://doi.org/10.1109/JPHOTOV.2011.2160489

[16] A. Sanchez, C. F. Davis Jr., K. C. Liu and A. Javan, "The MOM tunneling diode: Theoretical estimate of its performance at microwave and infrared frequencies", *J. Appl. Phys*. 49, 1978, pp. 5270 – 5277. https://aip.scitation.org/doi/10.1063/1.324426

[17] G. A. E. Vandenbosch and Z. Ma, "Upper bounds for the solar energy harvesting efficiency of nano-antennas", *Nano Energy* 1, 494–502, 2012. https://doi.org/10.1016/j.nanoen.2012.03.002

[18] E. Fournier and T. Bayne, "Under Hood Temperature Measurements of Four Vehicles," MVFRI, 2004. http://depts.washington.edu/vehfire/ignition/autoignition/surftemperdetail.html, Accessed online: 8 July, 2018.

[19] Z. Ma and G. A. E. Vandenbosch, "Optimal solar energy harvesting efficiency of nano-rectenna systems", *Solar Energy* 88, 163 – 174, 2013.

[20] E. Donchev, J. S Pang, P. M. Gammon, A. Centeno, F. Xie, P. K. Petrov, J. D. Breeze, M. P. Ryan, D. J. Riley and M. N. Alford, "The rectenna device: From theory to practice (a review)", *MRS Energy & Sustainability A Review Journal*, https://doi.org/10.1557/mre.2014.6

[21] J. R. Tucker and M. F. Millea, "Photon detection in nonlinear tunnelling devices," *Appl. Phys. Lett.*, vol. 33, no. 7, pp. 611–613, Oct. 1978.

[22] S. Grover and G. Moddel, "Metal Single-Insulator and Multi-Insulator Diodes for Rectenna Solar Cells", in *Rectenna Solar Cells*, Moddel G., Grover S. (eds). New York, NY, USA: Springer, 2013, ch. 6, pp. 89-109.

[23] Shilpi, K. Bhatt, Sandeep, S. Kumar and C. C. Tripathi (2017). Potential Challenges and Issues in Implementation of MIM Diodes for Rectenna Application. Presented at ICICCT. [Online]. Available: doi: 10.1109/ICICCT.2017.7975164

[24] S. R. Kasjoo, Z. Zailan, N. F. Zakaria, M. M. Isa, M. K. M. Arshad, and S. Taking, (2017). An Overview of Self-switching Diode Rectifiers Using Green Materials. Presented at 3rd Electronic and Green Materials International Conference, EGM 2017. [Online]. Available: https://doi.org/10.1063/1.5002451

[25] C. Balocco, S. R. Kasjoo, X. F. Lu, L. Q. Zhang, Y. Alimi, S. Winnerl, and A. M. Song, "Room-temperature operation of a unipolar nanodiode at terahertz frequencies," *Appl. Phys. Lett.*, vol. 98, May 2011. [Online]. Available: http://dx.doi.org/10.1063/1.3595414

[26] A. Westlund, "Self-switching Diodes for Zero-Bias Terahertz Detection", Ph.D. dissertation, Department of Microtechnology and Nanoscience – MC2, Chalmers University of Technology, Gothenburg, Sweden, 2015. Online: http://publications.lib.chalmers.se/records/fulltext/214629/214629.pdf&ved=2ahUKEwiHsZfWhcPfAhWosqOKHYTUApcOFjAFegOIAxAB&usg=AOvVaw0bcS567z3mOdS6vOGka8s0

[27] Y. Zhang, R. Han, Y. Kim, D. Y. Kim, H. Shichijo, S. Sankaran, C. Mao, E. Seok, D. Shim and K. O. Kenneth, "Schottky Diodes in CMOS for Terahertz Circuits and Systems", IEEE 13th Topical Meeting on Silicon Monolithic Integrated Circuits in RF Systems, pp. 24-26, January 2013. [Online]. Available: http://dx.doi.org/10.1109/SiRF.2013.6489420.

[28] H. Kazemi, K. Shinohara, G. Nagy, W. Ha, B. Lail, E. Grossman, G. Zummo, W. R. Folks, J. Alda and G. Boreman, "First THz and IR characterization of nanometer-scaled antenna-coupled InGaAs/InP Schottky diode detectors for room temperature infrared imaging," *Infrared Technol. Appl. XXXIII*, vol. 6542, no. 1, 65421J, 4 pp., 2007.

[29] T. W. Crowe, W. C. B. Peatman, P. A. D. Wood and X. Liu, "GaAs Schottky barrier diodes for THz applications", *Microwave Symposium Digest, 1992., IEEE MTT-S International*, pp. 1141 - 1144 vol.2, 1-5 June, (1992).

[30] B. H. Strassner and K. Chang, "Rectifying antennas (rectennas)," in *Encyclopaedia of RF and Microwave Engineering*, Hoboken, NJ: Wiley, 2005, p. 4418.

[31] E. R. Brown, "A system-level analysis of Schottky diodes for incoherent THz imaging arrays," *Solid-State Electron.*, vol. 48, pp. 2051–2053, Mar. 2004.

[32] K. J. Siemsen and H. D. Riccius, "Experiments with point-contact diodes in the 30-130 THz region," *Appl. Phys. A*, vol. 35, no. 3, pp. 177-187, Nov., 1984. http://dx.doi.org/10.1007/BF00616972

[33] L.E. Dodd, A. J. Gallant and D. Wood, “Controlled reactive ion etching and plasma regrowth of titanium oxides of known thickness for production of metal-oxide-metal (MOM) diodes”, *IET Micro and Nano Letters*, vol. 8, pp. 476-478, August 2013, DOI: 10.1049/mnl.2013.0177.

[34] D. Etor, “Optimising the Structure of Metal-Insulator-Metal Diodes for Rectenna Applications”, Ph.D. dissertation, School of Engineering and Computing Sciences, Durham Univ., Durham, UK, 2016. Online: http://etheses.dur.ac.uk/11903/

[35] P. Fontaine, D. Goguenheim, D. Deresmes and, D. Vuillaume, “Octadecyltrichlorosilane monolayers as ultrathin gate insulating films in metal-insulator-semiconductor devices,” *Appl. Phys. Lett*., vol. 62, No. 18, pp. 2256 – 2258, May, 1993, https://doi.org/10.1063/1.109433

[36] R. L. Bailey, “A proposed new concept for a solar-energy converter” *J. Eng. Power*, 94, pp. 73 – 77, 1972.

[37] J. C. Fletcher and R. L. Bailey, “Electromagnetic wave energy converter,” U.S. Patent 3 760 257, 1973.

[38] G. Droulers, A. Beaumont, J. Beauvais and D. Drouin, “Spectroscopic ellipsometry on thin titanium oxide layers grown on titanium by plasma oxidation,” *J. Vac. Sci. Technol. B*, 29, (2), pp. 021010-1 – 021010-6, Mar/Apr., 2011.

[39] M. N. Gadalla, M. Abdel-Rahman, A. Shamim, “Design, optimization and fabrication of a 28.3 THz nanorectenna for infrared detection and rectification”. *Sci. Rep.*, 4, 4270, doi: 10.1038/srep04270, 2014.

[40] P. Periasamy, J. D. Bergeson, P. A. Parilla, D. S. Ginley and R. P. O’Hayre, “Metal-insulator-metal point-contact diodes as a rectifier for rectenna”, in: *Proc. of 35th IEEE PVSC*, pp. 1858–1861, 2010. https://ieeexplore.ieee.org/document/5614531/

[41] P. Periasamy, J. J. Berry, A. A. Dameron, J. D. Bergeson, D. S. Ginley, R. P. O’Hayre and P. A. Parilla “Fabrication and Characterisation of MIM diodes based on Nb/Nb2O5 via a rapid screening technique”, *Adv. Mater.* vol. 23, 3080 – 3085, 2011.

[42] P. Periasamy, C. E. Packard, R. P. O’Hayre, J. J. Berry, P. A. Parilla and D. S. Ginley, “A novel way to characterize metal-insulator-metal devices via nanoindentation”, PVSC 37, 2011. [Online]. Available: https://ieeexplore.ieee.org/document/6186293/

[43] P. Periasamy, M. S. Bradley, P. A. Parilla, J. J. Berry, D. S. Ginley, R. P. O’Hayre and C. E. Packard, “Electromechanical tuning of nanoscale MIM diodes by nanoindentation”, *J. Mater. Res.* vol. 28 (14), 1912 – 1919, 2013. https://doi.org/10.1557/jmr.2013.171

[44] S. Krishnan, E. Stefanakos and S. Bhansali, "Effects of dielectric thickness and contact area on current-voltage characteristics of thin film metal-insulator-metal diodes", *Thin Solid Films*, 516, 2244 – 2250, 2008. https://doi.org/10.1016/j.tsf.2007.08.067

[45] M. Dragoman and M. Aldrigo, "Graphene rectenna for efficient energy harvesting at terahertz frequencies," *Appl. Phys. Lett.*, vol. 109, No.113105, Sept, 2016, https://doi.org/10.1063/1.4962642

[46] E. C. Anderson and B. A. Cola, "Photon-Assisted Tunnelling in Carbon Nanotube Optical Rectennas: Characterization and Modelling," *ACS Appl. Electron. Mater.*, April, 2019. Accessed on: April, 16th, 2019, DOI: 10.1021/acsaelm.9b00058 [Online].

[47] E. W. Cowell III, N. Alimardani, C. C. Knutson, J. F. Conley Jr., D. A. Keszler, B. J. Gibbons and J. F. Wager, "Advancing MIM Electronics: Amorphous Metal Electrodes," *Adv. Mater.*, vol. 23, pp. 74-78, 2011, DOI: 10.1002/adma.201002678.

[48] G. Auton, D. B. But, J. Zhang, E. Hill, D. Coquillat, C. Consejo, P. Nouvel, W. Knap, L. Varani, F. Teppe, J. Torres and A. Song, "Terahertz Detection and Imaging Using Graphene Ballistic Rectifiers," *Nano Lett.*, vol. 17, pp. 7015-7020, Oct., 2017, DOI: 10.1021/acs.nanolett.7b03625.

[49] C. Balocco, A. M. Song, M. Åberg, A. Forchel, T. González, J. Mateos, I Maximov, M. Missous, A.A. Rezazadeh, J. Saijets, L. Samuelson, D. Wallin, K. Williams, L. Worschech and H. Q. Xu, "Microwave Detection at 110 GHz by Nanowires with Broken Symmetry," *ACS Nano Lett.*, vol. 5, no. 7 pp. 1423-1427, Jul., 2005, DOI: 10.1021/nl050779g

[50] C. Balocco, M. Halsall, N. Q. Vinh and A. M. Song, "THz operation of asymmetric-nanochannel devices," *J. Phys.: Condens. Matter,* vol. 20, no. 384203 pp. 1-5, Aug., 2008, doi:10.1088/0953-8984/20/38/384203

[51] W. C. Brown, "The history of wireless power transmission", *Solar Energy* vol. 56, 3-21, 1996.

[52] S. Yan, B. Tumendemberel, X. Zheng, V. Volskiy, G. A. E. Vandenbosch, V. V. Moshchalkov, "Optimizing the bowtie nano-rectenna topology for solar energy harvesting applications", solar energy, Elsevier, vol. 157, 259-262, 2017. https://doi.org/10.1016/J.SOLENER.2017.08.035

[53] F. C. Chiu, "A Review on Conduction Mechanisms in Dielectric Films," *Advances in Materials Science and Engineering*," vol. 2014, pp. 1-18, 2014.

[54] J. G. Simmons, "Conduction in Thin Dielectric Films," *J. Phys. D: Appl. Phys.* vol. 4, pp. 613-657, 1971.

[55] S. M. Sze, and Kwok K. Ng, *Physics of Semiconductor Devices* 3rd Ed., (New Jersey), USA: John Wiley & sons, 2007, chs. 1, 2, 3, 4, 6, 8.

[56] S. M. Sze, and M. K. Lee, *Semiconductor Devices, Physics and Technology*, International Student version, 3rd Ed., Singapore: John Wiley & sons, 2013, chs. 2, 3, 5, 7.

[57] W.C. Lee and C. Hu, "Modelling CMOS tunnelling currents through ultrathin gate oxide due to conduction-and valence-band electron and hole tunnelling," *IEEE Transactions on Electron Devices*, vol. 48, no. 7, pp. 1366–1373, 2001.

[58] N. Alimardani and J. F. Conley, Jr., "Enhancing metal-insulator-insulator-metal tunnel diodes via defect enhanced direct tunnelling," *Applied Physics Letters*, 105, 082902, 2014; doi: 10.1063/1.4893735

[59] R. H. Fowler and L. Nordheim, "Electron Emission in intense Electric fields", *Proc. R. Soc. London, Ser. A 119, 173, 1928,* http://www.jstor.orglstable/95023

[60] L. W Nordheim, "The effect of the image force on the emission and reflexion of electrons by metals", *Proc. R. Soc. London, Ser. A 121, 626, 1928*.

[61] R. Holm, "Thermionic and Tunnel Currents in Film-Covered Symmetric Contacts", *J. of Appl. Phy.*, 39, 3294, 1968. https://doi.org/10.1063/1.1656771.

[62] J. Maserjian, "Tunnelling in thin MOS structures", *J. Vac. Sci. Technol*. 11, 996, 1974. https://doi.org/10.1116/1.1318719

[63] A. Sommerfeld and H. Bethe, *Handbüch der, Physik, edited by H. Geiger and K. Schell,* Julius Springer-Verlag, Berlin, 1933, Vol. 24/2, p. 450.

[64] R. Holm, "The Electric Tunnel Effect across Thin Insulator Films in Contacts", *J. of Appl. Phy.*, 22, 569, 1951. https://doi.org/10.1063/1.1700008.

[65] John G. Simmons, "Generalized Formula for the Electric Tunnel Effect between Similar Electrodes Separated by a Thin Insulating Film", *J. Appl. Phys.,* 34, 1793, 1963; https://doi.org/10.1063/1.1702682

[66] John G. Simmons, "Electric Tunnel Effect between Dissimilar Electrodes Separated by a Thin Insulating Film", *J. Appl. Phys.,* **34**, 2581, 1963; https://doi.org/10.1063/1.1729774

[67] R. A. Millikan and C. C. Lauritsen, "Relations of Field-Currents to Thermionic-Currents", *Proc. Natl. Acad. Sci.*, 14 (1) 45-49, 1928. https://doi.org/10.1073/pnas.14.1.45.

[68] E. William Cowell, S. W. Muir, D. A. Keszler and J. F. Wager, “Barrier height estimation of asymmetric metal-insulator-metal tunneling diodes”, *J. Appl. Phys. 114, 213703 2013;* https://doi.org/10.1063/1.4839695

[69] J. Jin, L. Wang, Z. Zheng, J. Zhang, X. Hu, J. R. Lu, D. Etor, C. Pearson, A. Song, D. Wood, A. J. Gallant and C. Balocco, “Metal-insulator-metal diodes based on alkyltrichlorosilane self-assembled monolayers”, *AIP Advances* 9, 065017 2019. https://doi.org/10.1063/1.5100252

[70] S. Datta, “Nanoscale device modelling: the Green’s function method”, *Superlattices and Microstructures*, vol. 28, no. 4, Jul. 2000. https://doi.org/10.1006/spmi.2000.0920

[71] X. Guo-Hua and K. Higashitani “Formation of OTS Self-Assembled Monolayer on Glass Surface Investigated by AFM,” *Journal of Zhejiang University (SCIENCE)*, vol. 1, No.2, pp. 162- 170, 2000.

[72] Y. Song, R. P. Nair, M. Zou and Y. Wang, “Superhydrophobic Surfaces Produced by Applying a Self-Assembled Monolayer to Silicon Micro/Nano-Textured Surfaces,” Nano Res. vol. 2, pp. 143-150, 2009; doi: 10.1007/s12274-009-9012-0.